Current and Temperature Variability on the Continental Slope

S. A. Thorpe

Phil. Trans. R. Soc. Lond. A 1987 **323**, 471-517
doi: 10.1098/rsta.1987.0100

Phil. Trans. R. Soc. Lond. A **323**, 471–517 (1987) [471]
Printed in Great Britain

CURRENT AND TEMPERATURE VARIABILITY ON THE CONTINENTAL SLOPE

By S. A. THORPE†

Institute of Oceanographic Sciences, Wormley, Godalming, Surrey GU8 5UB, U.K.

(*Communicated by H. Charnock, F.R.S. – Received* 28 *October* 1986)

CONTENTS

---

† Present address: Department of Oceanography, The University, Southampton SO9 5NH, U.K.

Vol. 323. A 1574 37 [Published 12 October 1987]

Observations of temperature and currents have been made in the lower part of the water column on the western slope of the Porcupine Bank southwest of Ireland where the water depth is about 3500 m. Moored and lowered instruments were used to study the processes that may lead to mixing and diapycnal transfer. A poleward Eulerian mean flow of about 2.5 cm s^{-1} is found in the bottom 250 m, with current direction rotating anticlockwise as the bottom is approached. The shear between 30 and 90 m off the bottom is, on average, geostrophic and the temperature variation at a point averaged over several tidal cycles is dominated by along-slope advection. There is, however, considerable variability, with strong semidiurnal oscillations in both current and temperature. There is a downward phase propagation in temperature at these frequencies indicating the presence of baroclinic M_2 waves. It is possible that these are responsible for the apparent along and off-slope fluxes of heat that are observed. Fluctuations with periods of 5–6 days appear to propagate polewards along slope with phase speeds of about 13 cm s^{-1}, but have constant phase lines lying roughly north–south at an acute angle to the mean contours of the slope.

Profiles of potential temperature obtained by using a lowered conductivity, temperature and depth (CTD) instrument show the presence of frequent inversions in the lower 150 m, sometimes exceeding 30 m in height. A moored array of platinum resistance thermometers sampling at 10 s intervals indicates that the inversions are associated with the semidiurnal variability in temperature, the most frequent inversions occurring when the temperature 10 m off the bottom is greatest and when the temperature is falling at higher levels with a component of the current directed upslope. Indirect estimates of the vertical diffusivity and turbulent dissipation are derived from the observed scales of inversions and the overall stratification. These are subject to considerable uncertainty but suggest that the contribution to turbulence in the boundary layer from the inversions may exceed that supplied by the shear stress on the sea bed.

Sources in instability are discussed, and one is examined analytically. An exact steady or time-dependent solution of flow of a stratified fluid parallel to a sloping boundary is derived. Solutions in which the density remains statically stable are possible only when a rather delicate balance exists between flow, stratification and diffusion.

1. INTRODUCTION

It is apparent to anyone walking along a beach and observing the plunging and spilling breakers at its edge that processes at the boundaries of the ocean may be responsible for rather special effects, particularly for mixing across density surfaces. Longuet-Higgins (1970), for example, has argued that the production of turbulence in the surf zone is generally dominated by wave breaking rather than by the working of the stress on the sea bed. Whether the diapycnal mixing involved in the entrainment of air into the ocean, or the aerosol flux onto land, is predominantly caused by waves breaking near the sea shore or to the less regular (but not, at least in high winds, infrequent) wave breaking (white horses) far off-shore, is, however, a matter beyond the scope of this paper. Here we are concerned with the parallel and comparable, but different, processes of diapycnal mixing in the stratified water deep below the surface, especially neighbouring ocean boundaries and particularly near continental slopes. If, as we later conjecture and attempt to show in an example drawn from observations, the nature of motion in the water adjacent to a slope may at certain locations have some of the character of the surf zone at the edge of a beach with waves playing an important role, then the structure of, and mixing in, such boundary layers may differ radically from those in regions dominated by turbulence produced by shear stress on the sea bed.

The matter is of some importance because although the processes supporting a diapycnal diffusivity of about 1 $\mathrm{cm^2\,s^{-1}}$ required to satisfy an advective diffusive balance in deep water (Munk 1966) are yet to be accurately quantified, none of the possible candidates acting in mid-water, for example internal wave breaking or double diffusive instability, appear on close inspection able to provide a demonstrably large-enough flux. Attention has therefore been given to the possible alternative: that, as suggested by Munk and promoted by Armi (1978), boundary mixing may provide a large component of the total diapycnal flux in an ocean basin.

Although boundary mixing has been evoked to explain some of the features of the temperature and salinity relation in the ocean (see, for example, Minster 1985) there are, unfortunately, few direct observations that can help to establish its importance, or even describe the structure of the benthic boundary layer on a slope. Over rough topography, temperature profiles have been observed to become more irregular (Wunsch 1970; temperature profiles also became less regular in lakes as their sloping boundaries are approached, see Caldwell *et al.* 1978) and close to sloping topography the energy in the internal wave field is found to exceed that generally found in internal waves in the ocean interior (Wunsch 1976; Eriksen 1982). Bird *et al.* (1982) used a single mooring to measure the currents and temperature variation in the benthic boundary layer on the Bermuda Rise at depth of 4630 m where the bottom slope is about 2° and the mean current is large, having an average speed of 22 $\mathrm{cm\,s^{-1}}$ and exceeding the tidal currents of about 5 $\mathrm{cm\,s^{-1}}$. As in previous studies in shallow water (Kundu 1976), they found a counter-clockwise change in mean current direction as the bottom was approached, some 6° between 62 and 6.9 m off the sea bed. The thickness of the mixed layer adjacent to the bottom was not well established but it generally exceeded 12 m and sometimes possibly extended to 62 m. Currents increased with height off the sea bed from 0.6 m to 62 m. An estimate of the boundary layer thickness, h, of 41 m was obtained by using the formula

$$h = \frac{1.3u_*}{f(1+N^2/f^2)^{\frac{1}{4}}}, \tag{1}$$

derived by Weatherly & Martin (1978), where $u_* = \sqrt{(\tau/\rho)}$ is the friction velocity, related to the shear stress on the sea bed τ and density ρ, f is the local inertial frequency and N is the buoyancy frequency. A one-dimensional turbulent closure model derived by the same authors compared favourably with observations of currents at the mooring but failed to reproduce both the direction against height and the temperature changes, the latter presumably because of its disregard of advective changes. The processes leading to turbulent diffusion were not studied, but larger damping was found for the tidal components, and higher in the water column, than for the steady flow, and the presence of helical rolls was suggested to explain the failure of the model to predict the changes in current direction.

The role of slopes in reflecting internal waves and thereby promoting mixing has been examined by Eriksen (1985). His study is based on both estimates and observations. The former are based on a theory of wave reflections that result in large changes between the incident and reflected spectra. It is, however, observed (Eriksen 1982) that anomalies in internal-wave spectra are found only within a few hundred metres of sloping topography, and Eriksen argues that some of the energy flux dissipated in the adjustment will support diapycnal diffusion.

Several studies (see, for example, Barbee *et al.* 1975; DeWitt *et al.* 1986) have been made to examine internal tidal waves near continental slopes and their generation through local interactions with the barotropic tides. Baines (1974) has suggested on theoretical grounds that the internal tides may become unstable, promoting mixing. In an experiment lasting two months on the continental slope of the south of Cape Cod, Wunsch & Hendry (1972) found evidence of internal M_2 tide generation at a position where bottom slope, α, matches the slope of the internal-wave group velocity, β, that is where

$$\sin\alpha = \sin\beta \equiv [(\omega^2-f^2)/(N^2-f^2)]^{\frac{1}{2}}, \tag{2}$$

where ω is the tidal frequency. The mean flow was about 2.3 cm s^{-1} westward along the slope, but turned anticlockwise by 10° between 97 m and 10 m off the sea bed. They inferred that the bottom Ekman boundary layer was very thin, typically only 1.5 m in thickness, and that the eddy diffusion coefficient for momentum determined from the Ekman layer thickness was about 3 $cm^2\,s^{-1}$. The estimate of boundary-layer thickness is much less than the thicknesses of the uniform regions adjoining the sea bed found by Armi & D'Asaro (1980) on the Hatteras Abyssal Plain, or by Saunders (1983) and Thorpe (1983) on the Madeira Abyssal Plain. The diffusion coefficient is moreover significantly less than those generally found for the radioactive tracer radon in the deep-ocean boundary layer (Sarmiento *et al.* 1976); near equality of momentum and diffusion coefficients might be expected in the low Richardson number environment of the benthic boundary layer (Turner 1973; see figure 5.13). Marsden (1986) has recently provided evidence to suggest that breaking of internal tides is responsible for mixing below the seasonal thermocline at shallow depths on the Georges Bank.

None of these studies were, however, designed to examine specifically the structure of the boundary layer on a slope and the general processes that lead to mixing or the consequences of mixing on the local dynamics. They do suggest, however, that the character of a boundary layer on a slope might, in some circumstances, be very different from those normally encountered, in that the production of turbulence might not result primarily from the work done on the fluid by the bottom stress, a source at the boundary, but from breaking internal waves, a source distributed in the vertical (Thorpe 1987).

The problem of studying the region more thoroughly has been partly because of inadequate instrumentation and partly the lack of a method or theoretical basis on which to base estimates of mixing. In consequence, boundary layers on slopes have been given less attention than they deserve, particularly in view of their possible effects in the dispersion of waste material dumped in the deep ocean, sediment stability and the production of nephel layers (Dickson & McCave 1986), and their importance to benthic fauna.

We have made observations on the slope west of the Porcupine Bank southwest of Ireland (figure 1), a region close to, but deeper than, that of Dickson & McCave's studies, where the bathymetry is well known thanks to coverage by a French 'Seabeam' survey. The topography

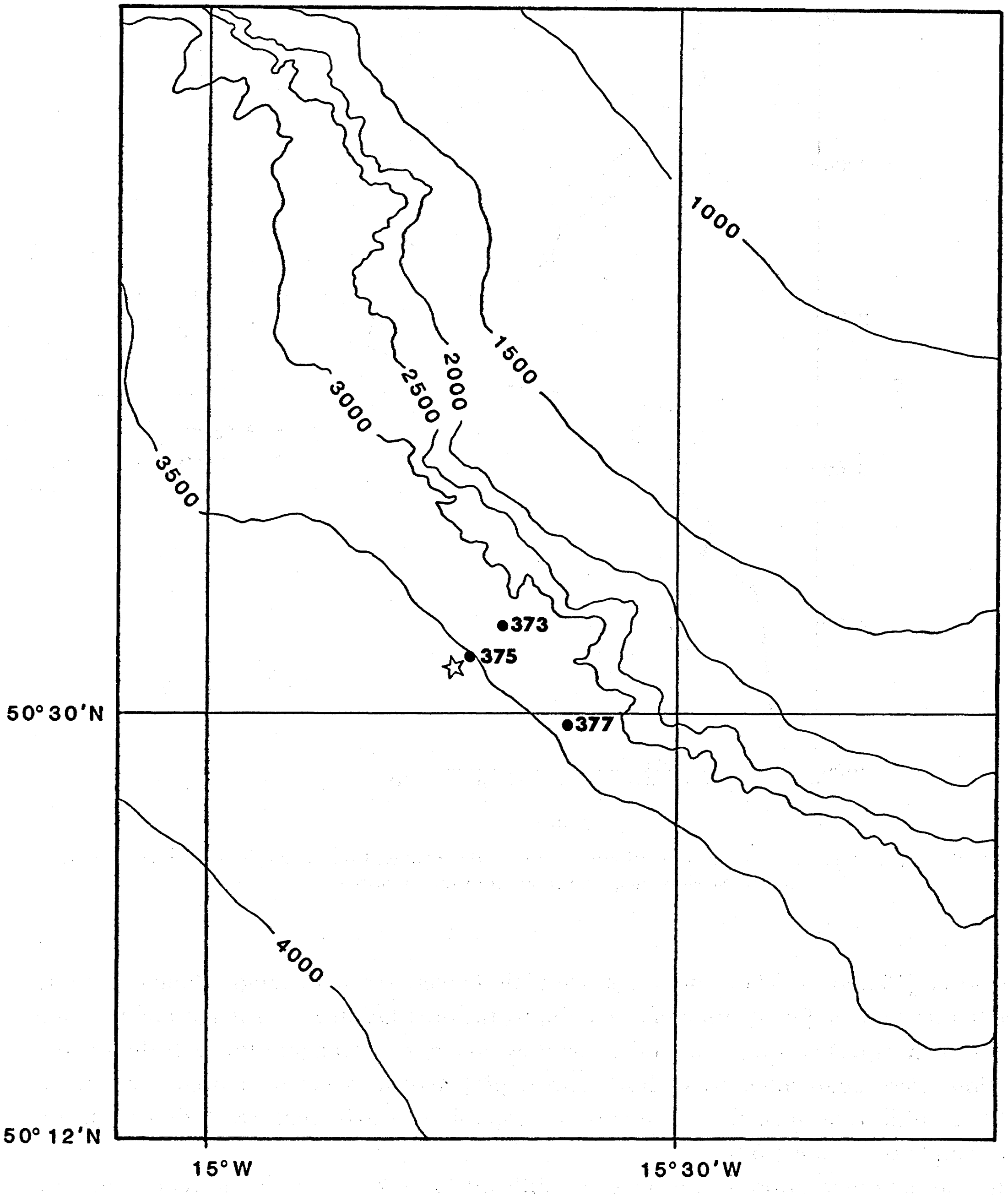

FIGURE 1. The observation area. Contour depths are shown in metres. The numbered points mark the positions of moorings. The significance of the position marked by the star is explained in §3.3.

is dominated by the steep gradients of the continental slope. The mean bottom slope, α, below 1500 m shown in figure 2 approaches 12° at 2500 m and is 3° at 3200 m. The along-slope topography is irregular, being marked on a SE–NW line through the moorings by undulations of wavelength about 3–5 km and height of 50–200 m. The instrumentation used was largely conventional, including a CTD survey in September 1984 (see §2), and the deployment of three moorings with VACM and Anderaa current meters for 245 days between September 1984 and

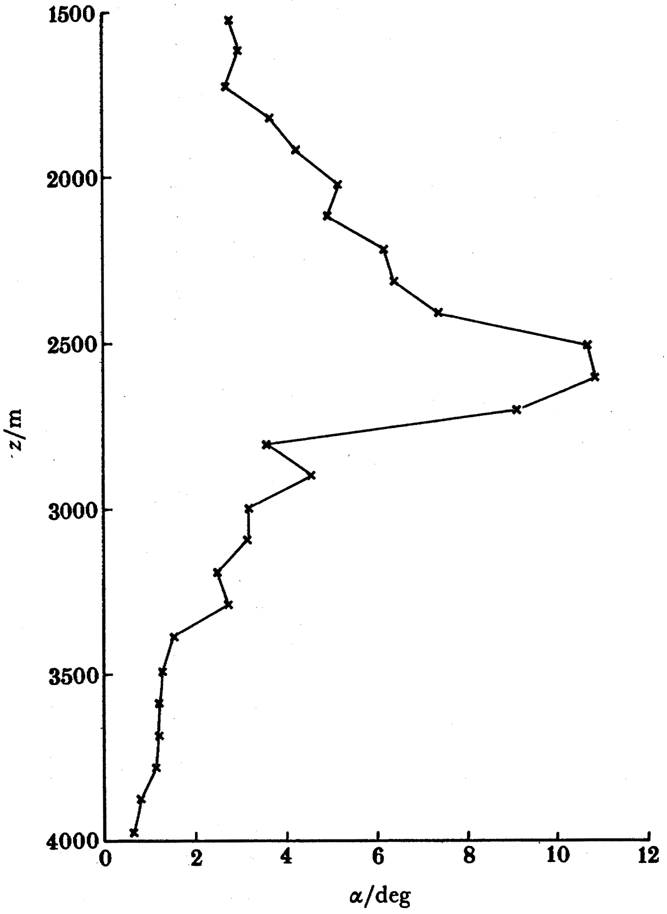

FIGURE 2. The mean slope angle, α, as a function of depth, z, determined from four echo sounding sections across the slope near the position of the moorings.

May 1985 (see §§3 and 4). These moorings (see table 1) were set in a triangle elongated along the slope (figure 1) with the intention of thus defining the orientation and propagation direction of features, such as fronts, waves, or eddies, as they advect or propagate through the region. Observations were augmented by a short-term deployment of a novel moored instrument, 'BERTHA' (benthic resistance thermistor array), capable of rapid, high-resolution measurements of temperature (see § 5.2).

Oceanographic observations of this kind are difficult to make, expensive to repeat and are seldom fully sufficient for the intended purpose. This is the case here. Although some conclusions can be drawn about the mean conditions and the nature of the variability, the observations fall short of a complete description of the boundary-layer structure. We offer this analysis of the data in the spirit of demonstrating what has been done and, more importantly, what might be done if more thorough measurements could be made. We have also advanced a theory of the structure of the slope boundary layer and this, and the stability of the density field in a steady or variable current adjacent to a sloping boundary, are described in §6.

Table 1. Current-meter data

oring er and .s. ref	position N	position W	water depth m		duration days	height off bottom m	currents (m s^{-1}) mean E	currents mean N	currents s.d. E	currents s.d. N	temperature °C mean	temperature °C 10^2 s.d.
373	50° 33.4′	14° 41.4′	3314	A	242	501	−0.48	1.30	7.94	6.72	2.893	4.43
				V	245	90	−2.05	1.44	5.65	4.20	2.651	4.34
				V	245	70	−2.10	1.37	5.57	4.27	2.641	4.49
				V	245	50	−2.28	1.52	5.63	4.68	2.631	4.63
				V	245	30	−2.61	1.37	5.52	4.91	2.622	4.81
				V	101	10	−2.48	0.28	4.92	5.07	2.619	5.37
375	50° 32.3′	14° 43.3′	3567	A	244	503	−0.64	0.87	4.54	4.15	2.767	3.92
				A	218	302	−0.57	1.07	5.04	3.93	F	F
				V	244	281	−0.53	0.81	5.19	4.11	2.641	3.59
				V	244	50	−1.02	2.27	5.54	5.70	2.517	3.40
377	50° 29.6′	14° 37.2′	3434	A	244	500	−0.80	1.27	4.53	4.70	2.924	3.99
				A	141	300	−0.91	1.98	4.78	4.55	2.723	4.42
				A	115	150	−1.25	2.20	4.32	4.26	2.648	4.90

Abbreviations: V = VACM, A = Aanderaa, F = faulty data. The VACMS recorded every half hour and the Aanderaas every hour.

2. T–S STRUCTURE

2.1. CTD *observations*

Figure 3 shows profiles of temperature and salinity at 50° 36.2′ N, 15° 19.2′ W made in September 1984. The water column between 700 and 1400 db† is strongly influenced by the presence of the high-salinity water originating from the Mediterranean. Beneath this is Labrador Sea water overlying the NE Atlantic Deep water below about 2000 db. The salinity maximum near 2500 db derives from water overflowing from the Norwegian Sea to the north. We are concerned principally with the water column below this maximum. Here the T–S relation appears to be very stable with salinity decreasing with potential temperature at a rate of about 0.085‰ K^{-1}. The value of the parameter $R_\rho = \alpha_1 \Delta T/\beta \Delta S$, where $\alpha_1 \Delta T$ and $\beta \Delta S$ are the mean contributions to potential density from potential temperature and salinity, respectively, over the same depth increments, is about 2.44, so that it is temperature rather than salinity that has the greater influence on density, temperature making a stabilizing and salinity a destabilizing contribution to static stability. The profiles may be unstable to double diffusive instability in the form of salt-finger convection (see §5.4). The mean buoyancy frequency, N, decreases with depth as shown in figure 4, having values of $(6\text{–}9) \times f$ (where f is about $1.12 \times 10^{-4}\ s^{-1}$) in the depth range for which data are available from moored instruments (see §§3 and 4). The corresponding internal Rossby radius, $Ro = NH/\pi f$, where H is the water depth, is about 7 km. CTD sections made across the slope between the 1250 m and 4100 m isobaths, roughly 15 and 30 km NW and SE of mooring 373, in September 1984, however, reveal no significant large-scale trends or horizontal features in the temperature–salinity distribution.

Figure 5 shows potential temperature profiles in the lower 400 db of the water column. The fairly uniform layers near the bottom found in the deeper water near 4000 m and commonly

---

† We have used both pressure (db) and length (m) as vertical scales, attempting to use whichever appears most natural. 1 db is approximately 0.983 m.

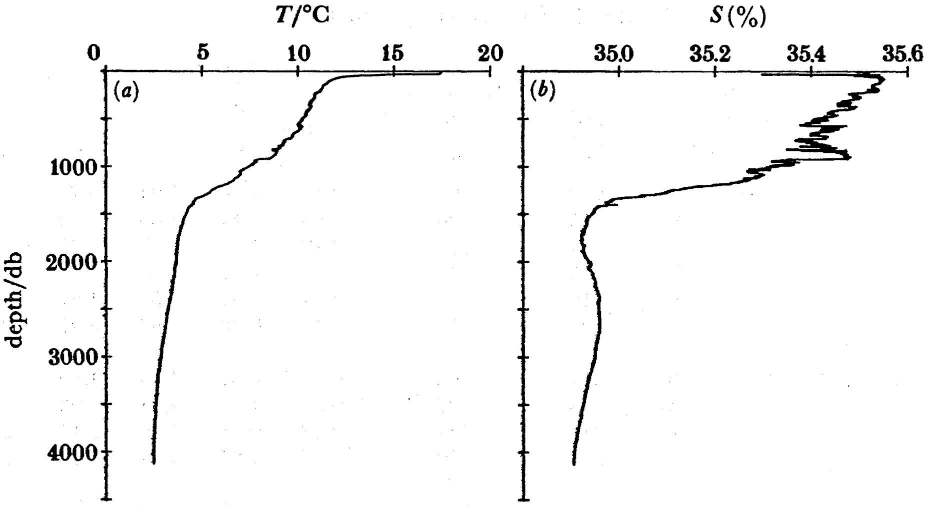

Figure 3. (*a*) Temperature and (*b*) salinity profiles typical of the observation area.

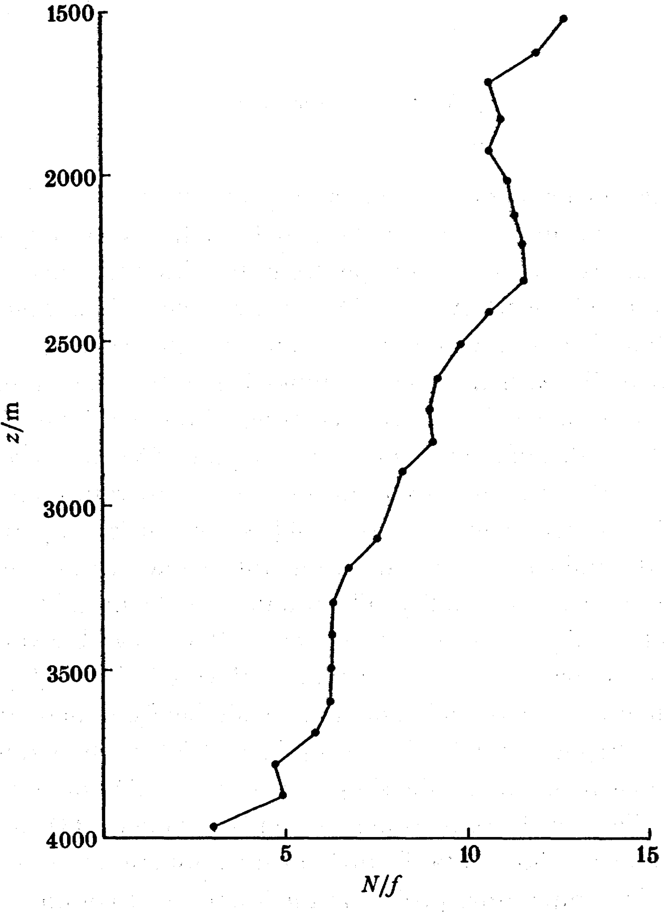

Figure 4. The mean buoyancy frequency, *N*, divided by the local Coriolis parameter, *f* ($1.12 \times 10^{-4}\ \mathrm{s^{-1}}$), as a function of depth, *z*.

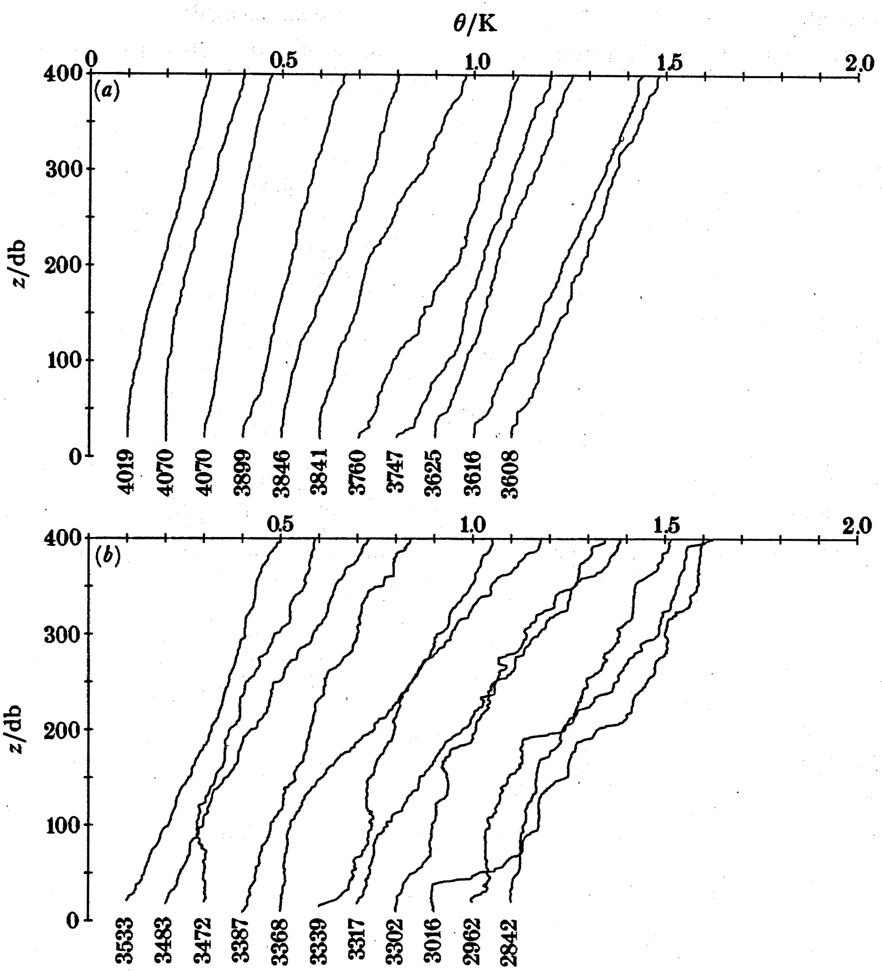

FIGURE 5. Profiles of potential temperature, θ, near the sea bed from (*a*) 4139–3644 m and (*b*) 3533–2845 m water depth. The depth is shown in metres below each profile and a relative temperature is given at the top.

occurring over abyssal plains (Armi & D'Asaro 1980) are more rare on the steeper slope, and here the temperature profile is more irregular, suggesting that mixing due to some process yet undetermined, may be occurring.

2.2. *Displacements*

Inspection of potential-temperature profiles near the mooring site shows that inversions occur. The vertical scale of these has been quantified by making estimates of the 'displacement scales' (see Thorpe 1977; Dillon 1982). We have selected for study a set of nine CTD casts made in the vicinity of the moorings and where the water depth is between 2800 and 3600 m. Here the influence of the Mediterranean water and the maximum in temperature or salinity at 2500 m (see figure 3) are negligible and produce no ambiguity in determining the displacements. Examples of the calculated displacements are given in figure 6. Although the measurement of salinity is generally less reliable than that of the temperature, being affected by the customary 'spikes' due to uncertain and inadequate temperature compensation in the processing, the larger inversions found in potential temperature can usually be recognized in the

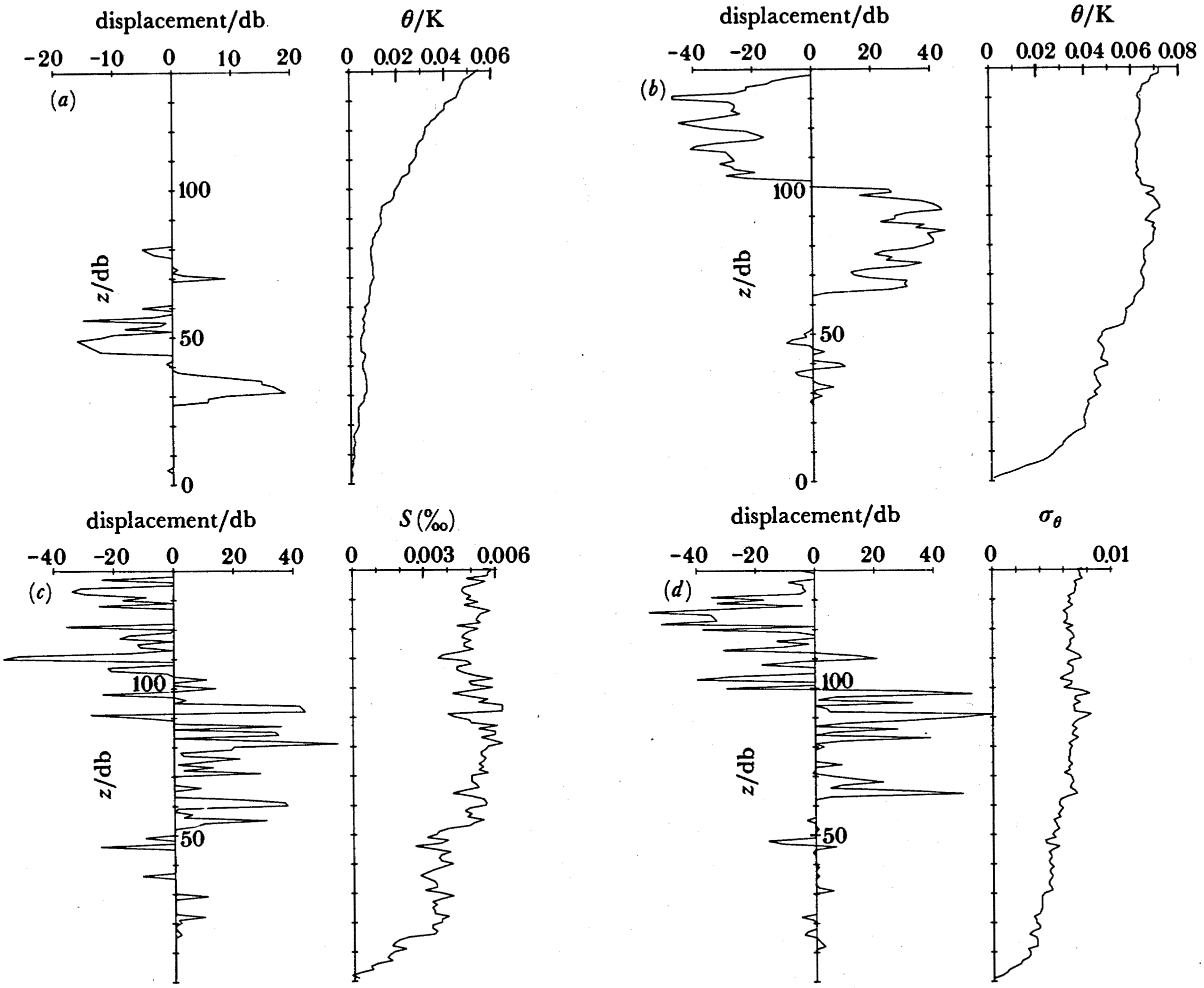

FIGURE 6. (*a*) and (*b*) show examples of displacements of potential temperature against height, *z*, in water depths of 3368 m and 3339 m, respectively. The displacements shown at the left of each section are found from the observed profile on the right by rearranging the measured values of potential temperature into a new profile in which the potential temperature decreases monotonically with depth. The vertical distances through which it is necessary to move each measured value is the displacement. The profiles end (*a*) 10 m and (*b*) 15 m off the sea bed, and the 'noise level' adopted is 0.5 mK. The potential temperature is plotted relative to that at the lowest point in the profile. (*c*) and (*d*) show the displacements of salinity, *S*, and potential density, σ_θ, of the CTD cast corresponding to (*b*). The noise levels are 5×10^{-4}‰ and 2×10^{-4}, respectively.

salinity and potential-density record (figure 6 *b–d*) showing that the observed features are not caused by temperature and salinity compensating intrusions (see, for example, Gregg 1975). (The figure shows an exceptionally large inversion and, generally, the inversions were about 2–4 m in scale.)

The original calculations of displacements (Thorpe 1977) were at shallow depths in a freshwater lake, where compressibility and salinity gradients could be neglected. In the deep ocean, potential density should, strictly, be used in place of temperature to calculate the displacements. In view of the uncertainty in the salinity estimates, and hence in those of potential density, we have, however, chosen to derive the mean displacements from the potential temperature alone, making the assumption that the *T–S* relation is stable. This provides the most reliable estimates from the available data. The rate of lowering of the CTD was 1–1.5 m s^{-1} but, because of ship motion, the instrument did not descend steadily through the water but occasionally lifted for brief periods, possibly disturbing the water through which it was subsequently again to descend. We have therefore accepted for analysis only those parts of the record for which pressure at the CTD was increasing and have ignored the parts for which the instrument was rising or subsequently redescending to a depth previously achieved during the cast. The data set thus produced is of samples in undisturbed water. Samples are taken at depth intervals of about 5 cm, and the time response of the sensor is about 180 ms. The data are now averaged into depth increments, D, the new set resorted so that potential temperature decreases with depth, and the displacements calculated as explained by Thorpe (1977) recognizing displacements only where the change in temperature exceeds a noise threshold, 0.5 mK†. The r.m.s. displacements, d, averaged over all the displacements (including zero values), have been found for various averaging increments, D. As D increases the estimates $d(D)$ decrease to zero because the overall profile is stable.

We find that provided the averaging increment is less than d, the value of d is fairly insensitive to the choice of D, and can be estimated to about 20% by averages over 1 db. This appears to be because the major contribution to d comes from relatively few but large displacements that dominate those from the more frequent, but small, displacements.

The variation in the r.m.s. displacements calculated in the bottom 150 m of the water column from each of the nine CTD casts is considerable, ranging from 0 to 31.3 m. The average is dominated by contributions from two CTD casts, each of which contained large displacements from a single overturning event (one is that shown in figure 6*b*). The mean over all nine is 15.1 m or, neglecting the two large contributions, 6.5 m. (If 'zero' displacements are neglected, the r.m.s. displacements are about 1.6 times greater.) These compare with values of order 1 m in water 250 m or more from the slope. The sample is unfortunately not sufficiently large for a precise estimate of the mean. It is, however, clear that large overturning events occasionally occur in the benthic boundary layer on the slope at heights that we shall show (§3.1) appear to be well above that of the estimated frictional boundary-layer thickness. We shall later (§§5–7) examine their cause.

3. THE MEAN FLOW

3.1. *Currents*

Details of the moorings and eulerian mean currents are given in table 1. Progressive vector diagrams are shown in figure 7 and the variation of mean current with height in figure 8. Currents are predominantly to the northwest parallel to the local isobaths, with stronger currents in the lower 200 m (compare 50 m and 281 m in figure 7*b* for mooring 375; currents increase with depth between 90 m and 10 m on mooring 373) suggesting the presence of a fairly narrow slope boundary-current. The general drift is consistent with that reported by Dickson *et al.* (1985) for the northeastern part of the Porcupine Abyssal Plain. A turning to the right with increasing distance from the bottom is consistent with other observations (see §1) but is

---

† The estimates of displacement are dependent on the 'noise level' above which differences in temperature are recognized. The r.m.s. displacements were found to increase roughly linearly and by a factor of about 2 as the 'noise level' was decreased from 1.5 to 0.5 mK. Below 0.5 mK the estimated displacements increased more rapidly. This value of 0.5 mK corresponds to the noise level of the CTD in well-mixed conditions and has been adopted in estimating the displacements.

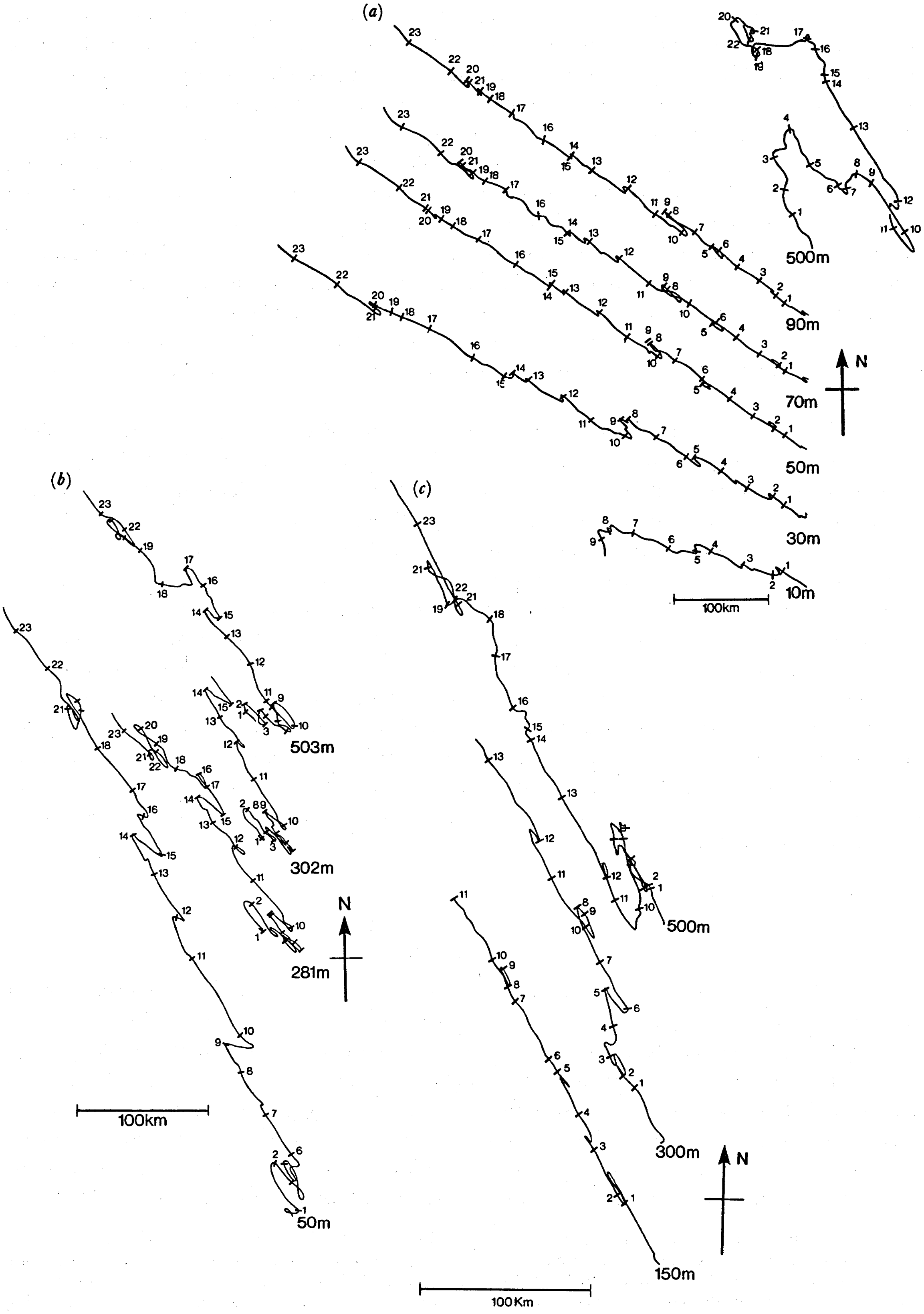

Figure 7. Progressive vector diagrams for instruments on mooring (*a*) 373, (*b*) 375 and (*c*) 377. Points are marked every 250 h and the vectors have been averaged over 25 h.

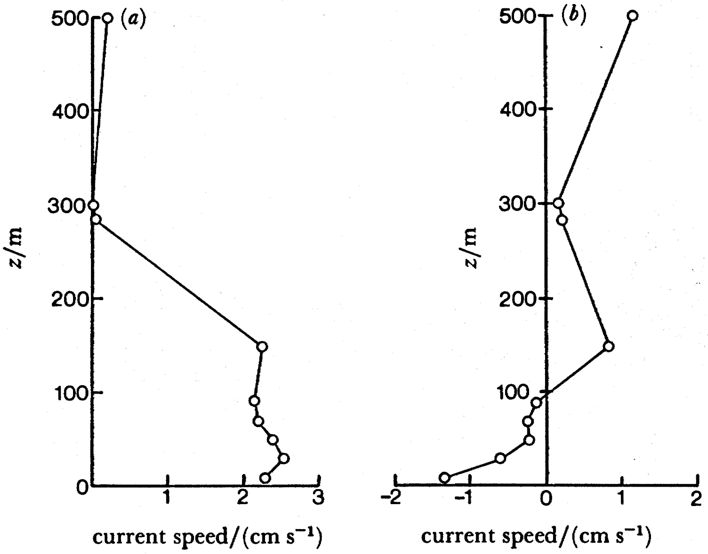

FIGURE 8. Mean variation of current with height above the sea bed over a period of 93.7 days, all instruments operating. (*a*) Along slope, 310°; (*b*) across slope, 040°.

more extreme than usual. During the simultaneous operation of instruments on mooring 373 (figure 8) the turning was 17.5° between 10 and 30 m, 8.5° between 30 and 50 m and 1° between 50 and 90 m (possible errors being about ±3°). The increase in mean current towards the bottom suggests that the frictional layer near the sea bed is not penetrated by the array, and this is consistent with a value of 5.8 m for the boundary layer thickness derived from (1) with a drag coefficient of 3×10^{-3} (Heathershaw 1979) and the mean currents used to estimate the friction velocity. For comparison, Bird *et al.* (1982) report a decrease of about 1 cm s^{-1} between 63 m and 12 m, and a 6.6 cm s^{-1} decrease between 12 m and 0.8 m. Similarly, Wunsch & Hendry (1972) found little mean shear between 97 and 10 m, but a 20% decrease in mean current between 10 and 2 m. Current reversals for periods of 5–7 days or so are observed (figure 7), similar to the reversals found by Wunsch & Hendry.

3.2. *Temperature*

The mean temperature profile measured by the instruments on mooring 373 showed no evidence of a mixed layer near the bottom, mean potential temperature decreasing steadily towards the sea bed.

3.3 *Geostropy*

We have examined the geostrophic balance by analysing data from moorings 373 and 375. These are set across the slope (figure 1) about 2.98 km apart, less than half the internal Rossby radius (§2.1). We determined the vertical gradient in current in a direction normal to the line joining the moorings from the difference in current components at 90 and 30 m on 373, Δv, and found the horizontal temperature gradient from the difference between an average at 30 and 50 m on 373 and at 281 m on 375, ΔT. The data were averaged over different time intervals and Δv plotted against ΔT. Examples are shown in figure 9, and the coefficients of the lines of best fit, $\Delta v = A + B\Delta T$ and regression coefficients are given in the caption. The generally

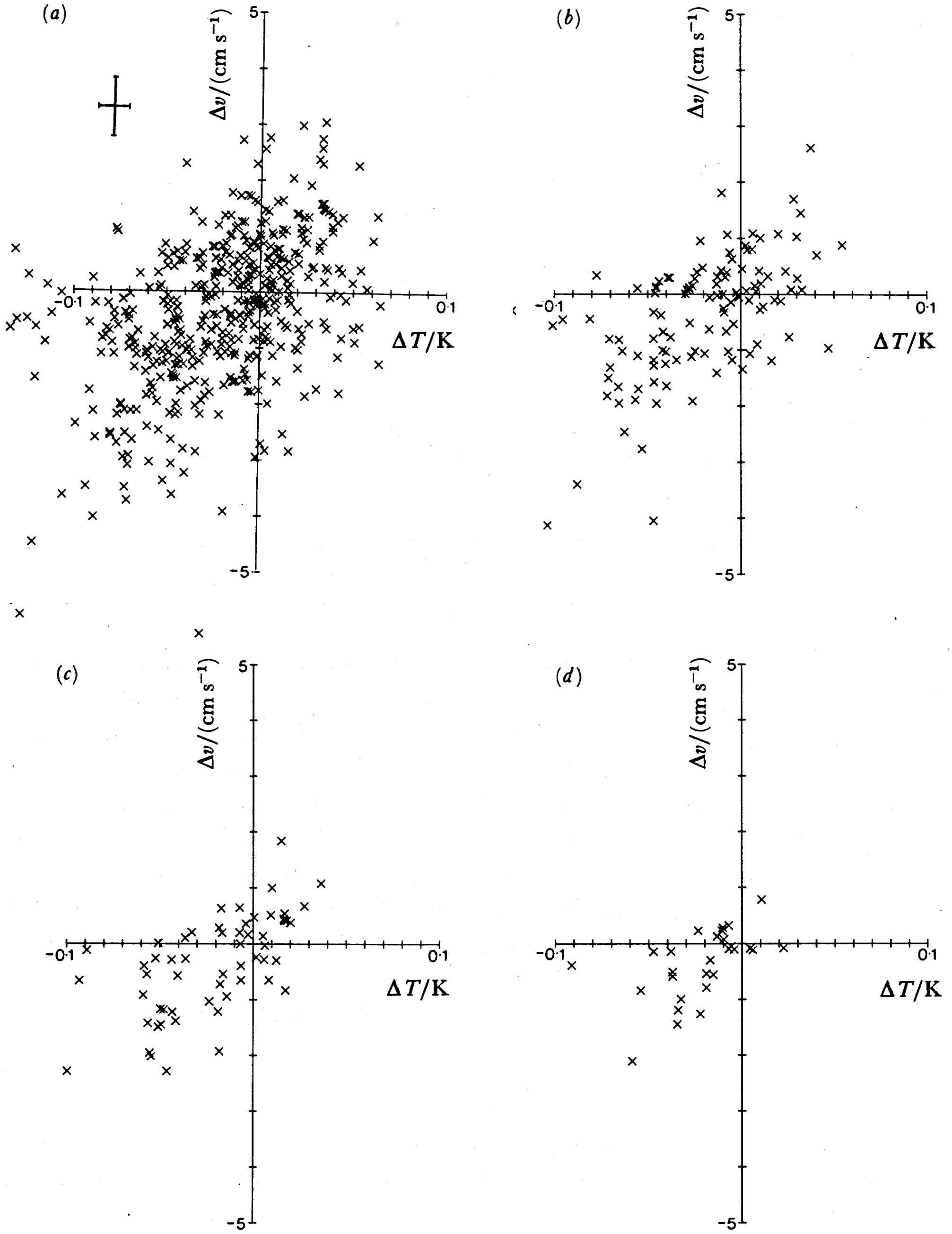

FIGURE 9. The difference, Δv, between the velocity component at 90 m and 30 m on mooring 373 normal to the line joining moorings 373 and 375, against the temperature difference, ΔT, between moorings 373 and 375, separated by 2.98 km, at a depth of 3286 m. Estimated error bars are shown in (*a*). The averaging intervals, the coefficients in lines of best fit $\Delta v = A + B\Delta T$, and the regression coefficients, r, are given in the table below.

	av. intervals h	no. samples	A (cm s^{-1})	B (cm s^{-1} K^{-1})	r
(*a*)	12.5	460	−0.0348	15.71	0.45
(*b*)	50	115	0.0043	17.62	0.57
(*c*)	100	57	0.0065	19.73	0.64
(*d*)	200	28	−0.0564	14.40	0.55

negative values of ΔT implies that the isopycnal surfaces near the slope are generally 'set-up', on average by about 48 m. A linear correlation between Δv and ΔT is significant at the 0.3 % level, and the coefficients A are close to zero, so that, on average, the shear reverses when the temperature gradient changes sign, but the scatter appears to increase as the averaging time decreases.

If Δz is the vertical distance over which Δv is estimated, and Δy is the horizontal distance over which a density difference $\Delta\rho$ corresponding to ΔT is measured, then, for geostrophic balance

$$\Delta v = -\frac{g}{f}\frac{\Delta z}{\Delta y}\frac{\Delta\rho}{\rho_0}, \tag{3}$$

where ρ_0 is a reference density and g is the acceleration due to gravity. If now $\rho = \rho_0(1-\alpha_1 T+\beta S)$, then

$$\frac{\Delta\rho}{\rho_0} = -\alpha_1 \Delta T\left(1-\frac{1}{R_\rho}\right), \tag{4}$$

so that

$$\Delta v = \frac{g\alpha_1}{f}\frac{\Delta z}{\Delta y}\Delta T\left(1-\frac{1}{R_\rho}\right) \tag{5}$$

or

$$\alpha_1\left(1-\frac{1}{R_\rho}\right) = \frac{f\Delta y}{g\Delta z}\frac{\Delta v}{\Delta T}. \tag{6}$$

Hence using the appropriate values $f = 1.12\times10^{-4}\ \mathrm{s^{-1}}$, $g = 9.81\ \mathrm{m\ s^{-2}}$, $\Delta z = 0.06$ km and $\Delta y = 2.98$ km, and estimating $\Delta v/\Delta T \approx B \approx 0.16\ \mathrm{m\ s^{-1}\ K^{-1}}$, we have $\alpha_1(1-1/R_\rho) = 9.07\times10^{-5}\ \mathrm{K^{-1}}$, so that if $R_\rho = 2.44$ (see §2.2), then $\alpha_1 = 1.5\times10^{-4}\ \mathrm{K^{-1}}$, and this is very close to the expected value $(1.61\times10^{-4}\ \mathrm{K^{-1}})$ at 2.65 K, 34.95‰ at 3000 m.

We conclude that the motion near the slope is principally in geostrophic balance. The estimates moreover lend support to the assumption that the T–S relation observed in the CTD survey remained stable throughout the mooring deployment period. The scatter of points in figure 9*d* may be because of ageostrophic motion (principally, it appears, at high frequency) or to short-term variation in the T–S relation. The former appears to be more likely.

The vertical component of vorticity relative to the Earth estimated from instruments at the same levels on each mooring, a depth of 3286 m, has a mean cyclonic component mainly from the contribution of the slope current of about $0.032f$ and, averaged over two semidiurnal M_2 tides, ranges from $-0.09f$ to $0.17f$. The apparent mean centre of rotation is at the position marked by a star in figure 1.

4. VARIABILITY: LONG-TERM TO TIDAL PERIODS

4.1. *Long-term variations*

Figure 10*a* shows 25 h average values of current and temperature at a height of 70 m on mooring 373. For simplicity, the currents have been divided into two components directed roughly along (direction 310) and across the isobaths (direction 040) that will be referred to as long-slope and *x*-slope currents, respectively. This record is characteristic of the other records, showing the predominantly long-slope variation in currents. The temperature at all instruments fell by about 0.1 K between 90 and 110 days after deployment but recovered between 130 and 150 days.

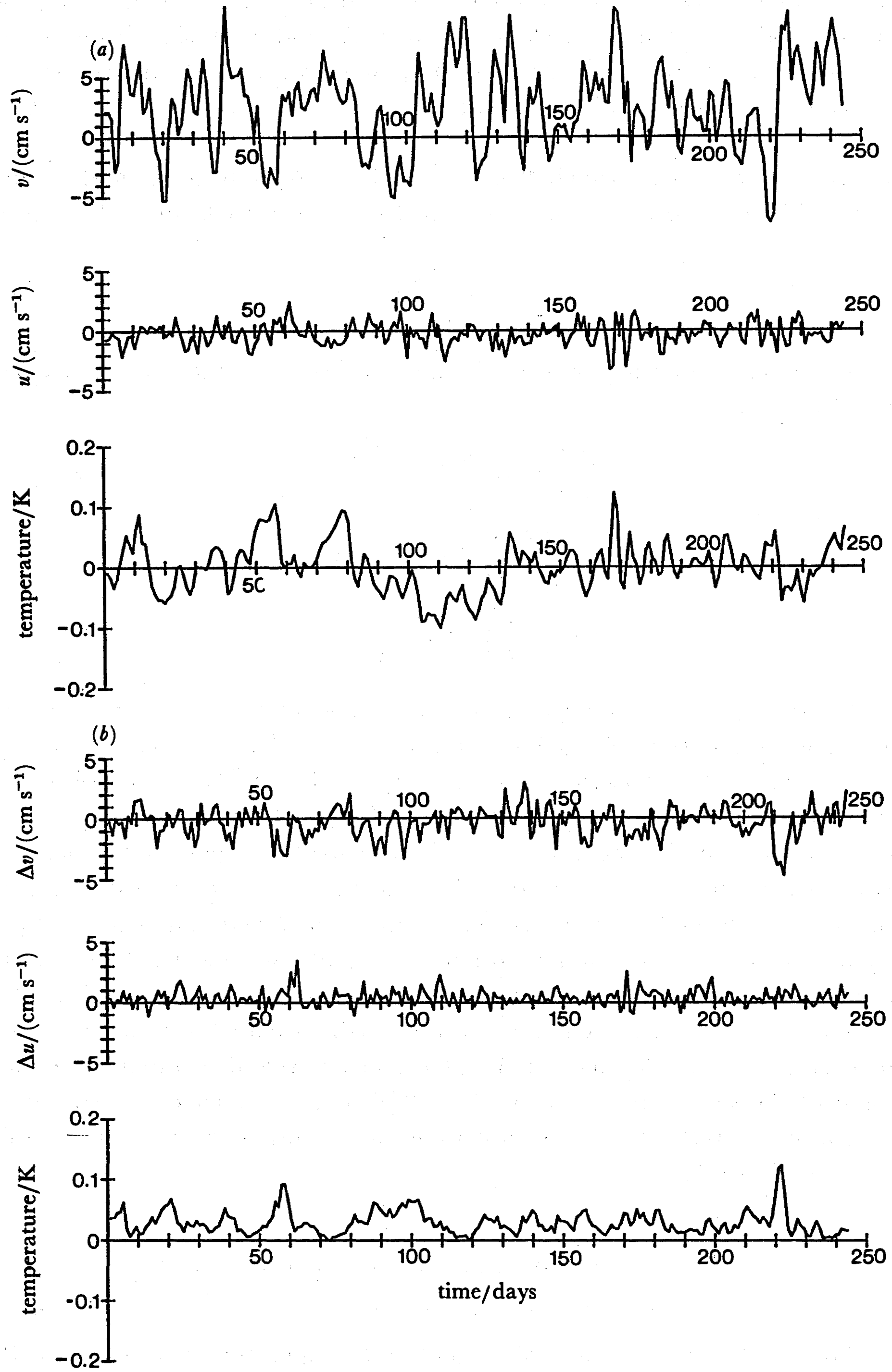

FIGURE 10. (*a*) 25 h averages of (top to bottom) long-slope (310°) current (mean current = 2.49 cm s^{-1}), *x*-slope (040°) current (mean current = −0.30 cm s^{-1}), and the temperature variation from the mean (2.6400 K) at 70 m off the sea bed at mooring 373. (*b*) 25 h average of the difference between (top to bottom) long-slope, *x*-slope currents and temperature at 90 m and 30 m off the sea bed at mooring 373.

Figure 10*b* shows the difference between the currents and temperature at 90 and 30 m off the bottom in mooring 373. The temperature is always positive, indicating that a mixed layer never extends to 90 m. The most obvious feature is the inverse relation between temperature gradient and long-slope shear, particularly conspicuous when the temperature gradient peaks near 58 and 221 days. This has implications for stability (see §4.5).

4.2. *Spectra of currents and temperatures*

Current spectra from instruments 281 m off the sea bed at mooring 375 and 30 m off the sea bed at mooring 373 are shown in figure 11, and temperature spectra are shown in figure 12. These two instruments, both VACMS, are at almost the same depths (3286 and 3284 m respectively) and are on a line roughly normal to the slope. All spectra show well-defined M_2 tidal peaks and lesser, but clear, peaks at first and second harmonics. A diurnal peak is apparent in the long-slope currents, and in the temperature spectra of the lower instruments at mooring 373.

Spectra at mooring 373 are marginally higher than those at 375 but the difference lies within the 95 per cent confidence limits. At frequencies between M_2 and N, spectra suggest equi-

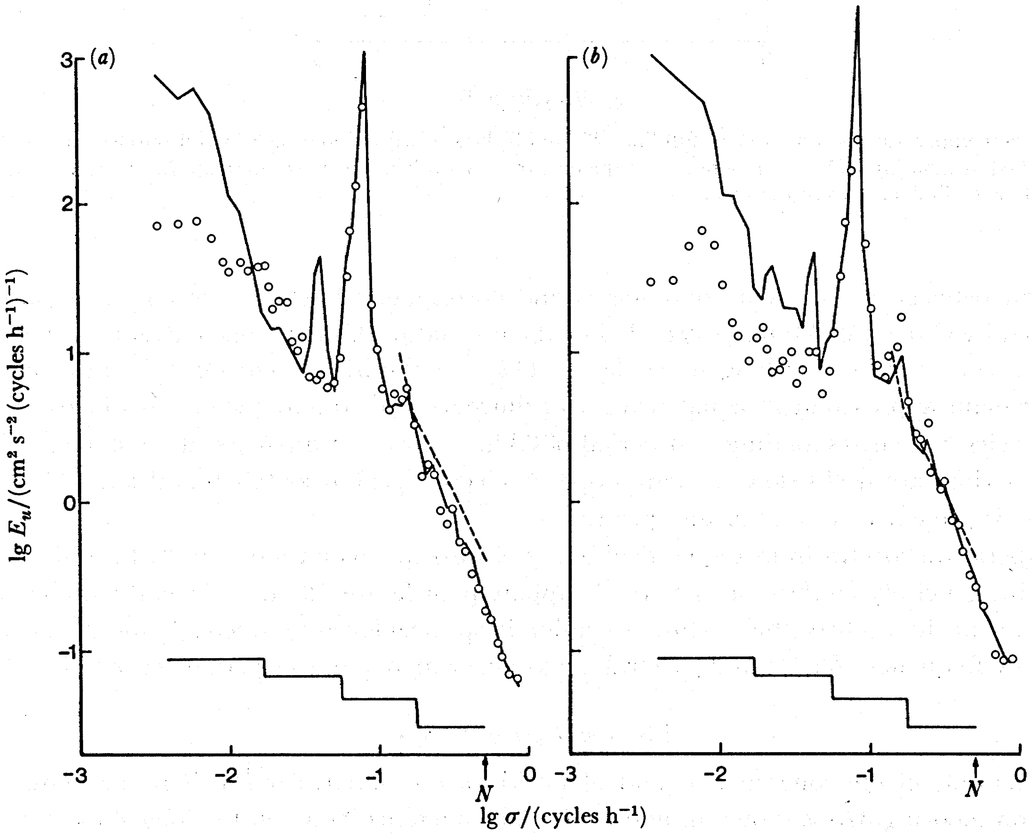

FIGURE 11. Power spectra of current (*a*) 281 m off the sea bed at mooring 375 and (*b*) 30 m off the sea bed at mooring 375 as a function of frequency, σ. The full line is the long-slope component, and the circles the x-slope component. The broken line shows a level corresponding to half that of the Garrett–Munk spectrum. Comparison between this and the observed data is valid if there is equipartition between the long-slope and x-slope components. The 95% confident bands are indicated by the stepped curve.

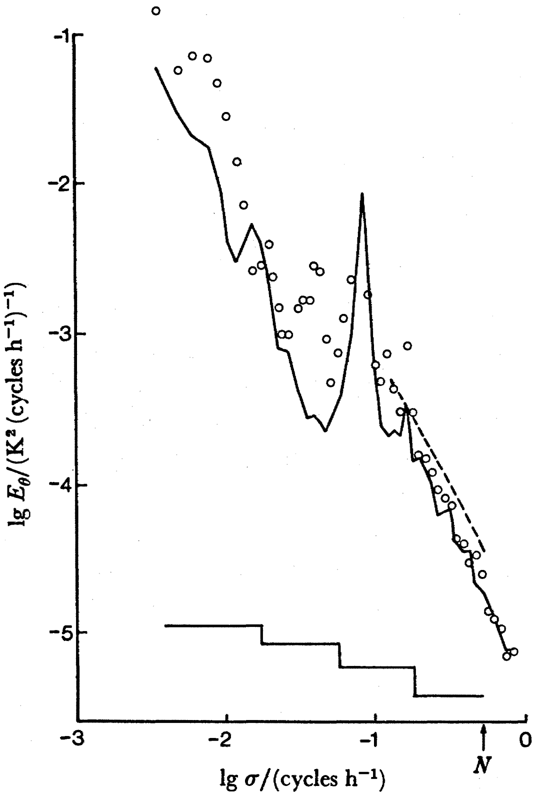

FIGURE 12. Temperature power spectra (full line) 281 m off the sea bed at mooring 375 and (circles) 30 m off the sea bed at mooring 375, as a function of frequency, σ. The broken line shows Garrett–Munk spectrum. The confidence limits are as in figure 11.

partition between the current components and correspond closely to the empirical spectra proposed by Garrett & Munk (1972). Below the diurnal peak the *x*-slope current spectrum at 373 lies below that of the long slope (figure 11*b*). At the instrument on 375, however, the levels remain approximately equal (except at diurnal) until the frequency falls below about 0.016 cycles h^{-1}, corresponding to a period of 63 h. At lower frequencies, the *x*-slope levels at both moorings are well below the long slope. A spectral peak near 0.008 cycles h^{-1} (5–6 day periods) is present in several of the spectra.

Temperature spectra from the vertical array of instruments on mooring 373 are shown in figure 13, generally confirming the trends apparent in figure 12: the diurnal component is stronger near the sea bed; there is little variation in spectral levels between M_2 and N, the local buoyancy frequency (§2.1); and spectral peaks occur at M_2 and at periods of 5–6 days.

4.3. *Coherence and phase*

An example of the coherence, c, and phase, ϕ, of the signals from a single instrument at 281 m on mooring 375 is shown in figure 14. The coherence between the long-slope currents and temperature is generally low with variable phase, an exception being at M_2 where the long-slope component leads the temperature by 102°. The *x*-slope currents generally lag the temperature by about 90°, consistent with a falling temperature as deeper-lying cold water is carried upslope by the *x*-slope current. (An exception is the peak in coherence at $\lg\sigma = -1.54$,

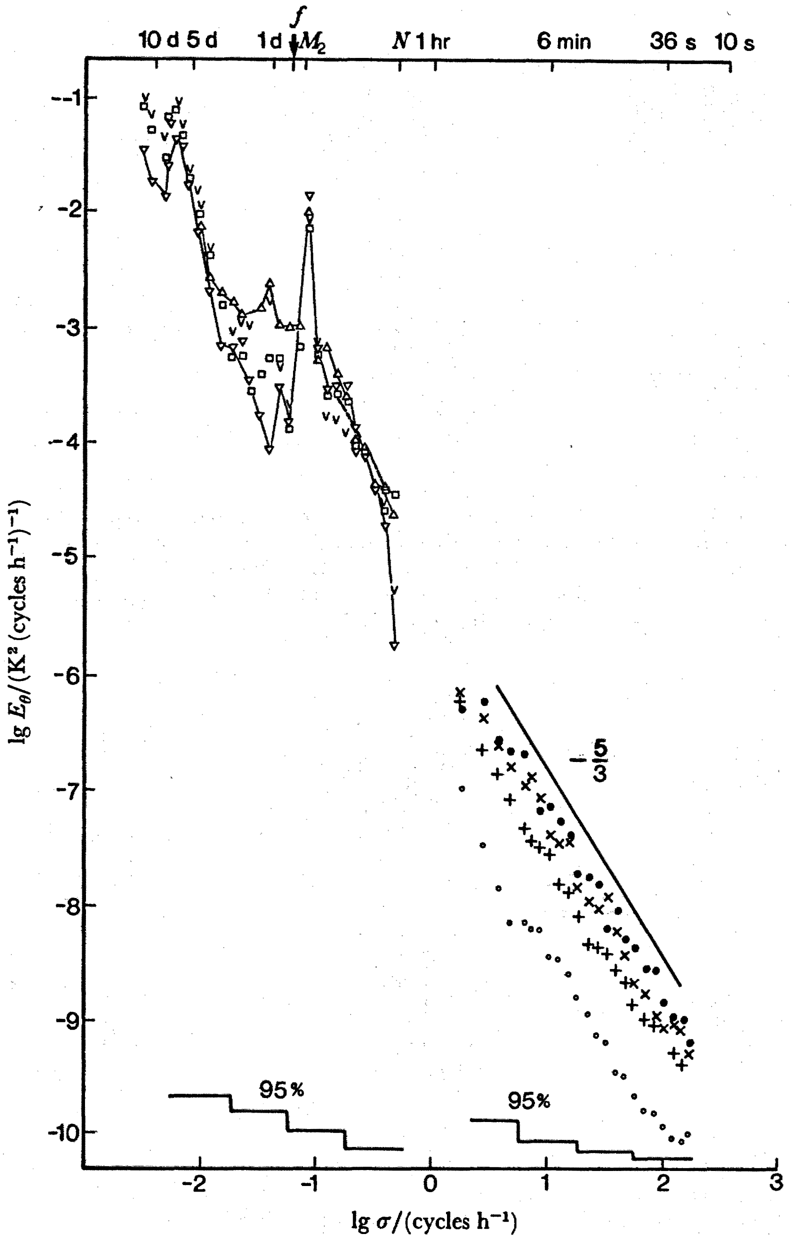

FIGURE 13. Temperature spectra from instruments on mooring 373 at (▽) 500 m, (□) 90 m, (v) 50 m and (△) 10 m. Spectra from BERTHA (figures 22 and 23) for period (●) A, (+) period B, (○) period C and (×), period D, are also shown, together with 95% confidence limits. The broken line shows the Garrett–Munk spectrum.

i.e. 34.3 h, where the lag is 28°; this peak is not, however, reproduced at other instruments.) The x-slope currents generally lag the long-slope currents, typically by 30–50° at the lowest frequencies and by 90° at frequencies exceeding M_2. The lag at M_2 is 178°. The correspondence lag at the instrument at 30 m on mooring 373 is 117°, but here the coherence between the components is only 0·29 and is barely significant, at the 95% level.

Examples of coherence and phase between instruments separated vertically and horizontally in a direction off-shelf are given in figures 15 and 16, respectively. Most notable in the vertically

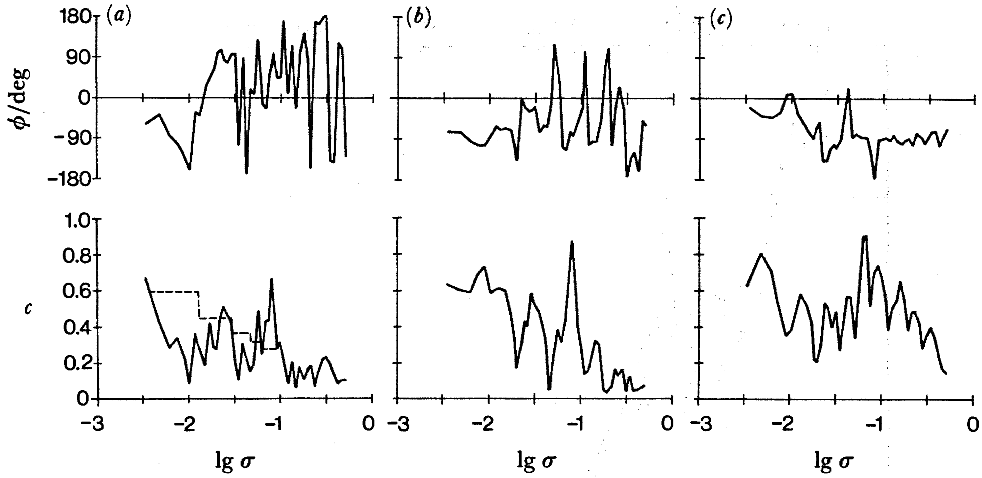

FIGURE 14. The phase, ϕ, and coherence, c, against $\lg \sigma$ (frequency, σ, measured in cycles h^{-1}) for (*a*) long-slope current against temperature, (*b*) *x*-slope current against temperature, and (*c*) *x*-slope current against long-slope current at the instrument at 281 m off the sea bed on mooring 375. The 95% confidence limits for coherence are shown by the broken lines in (*a*) and are identical in (*b*) and (*c*). Phase errors up to 30 min may occur because of uncertainty in recording times, but are generally less.

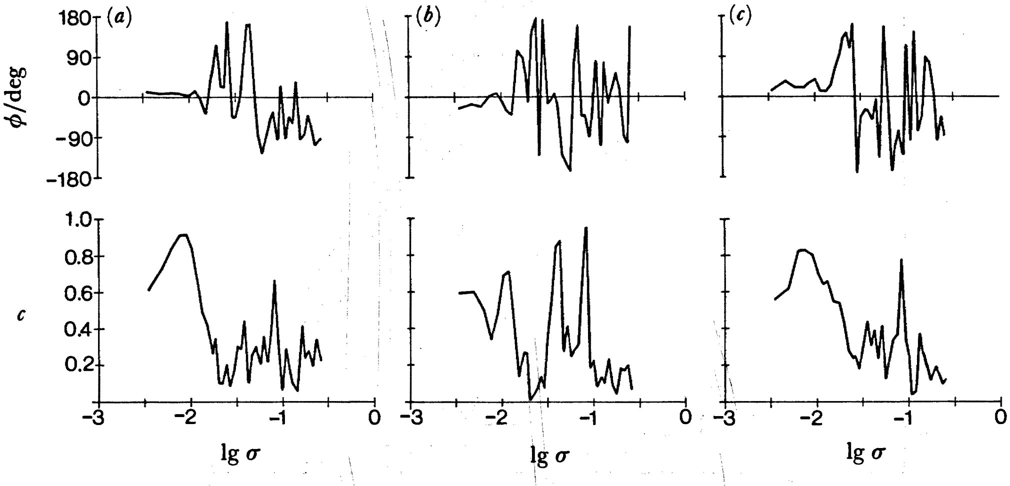

FIGURE 15. The phase, ϕ, and coherence, c, against $\lg \sigma$ (frequency, σ, measured in cycles h^{-1}) between (*a*) temperatures, (*b*) long-slope currents, and (*c*) *x*-slope currents at 501 m and 90 on mooring 373. Confidence limits as in figure 14*a*.

separated instruments on mooring 373 (figure 15) is the high coherence at periods of 5–6 days ($\lg \sigma \sim -2.2$) in temperature and *x*-slope current with small phase difference, the high coherence (with non-zero phase shifts in temperature) at M_2, and the high coherence with zero phase shift in the diurnal long-slope current. The latter coherence is absent in the temperature and *x*-slope components. These results, together with the spectra (figure 11), show that the diurnal tide is thus largely barotropic aligned along the topography. This orientation is in accordance with predictions based on Schwiderski's (1980*a*, *b*) barotropic tidal model. The ellipticity of the M_2 barotropic tide is predicted to be small with currents principally directed north–south. The records show evidence of a strong baroclinic component.

The coherence between instruments at 30 and 90 m is generally much higher than between those at 90 and 501 m (figure 15) and the phase differences are small, but the the main features of the coherence are similar. These are again reproduced when comparing instruments at the same depth but 3 km apart (figure 16) the principal change being in the phase variation. At low frequencies there is an apparent off-shore propagation, at diurnal the long-slope currents are nearly in phase, and at M_2 the phase advances on shore.

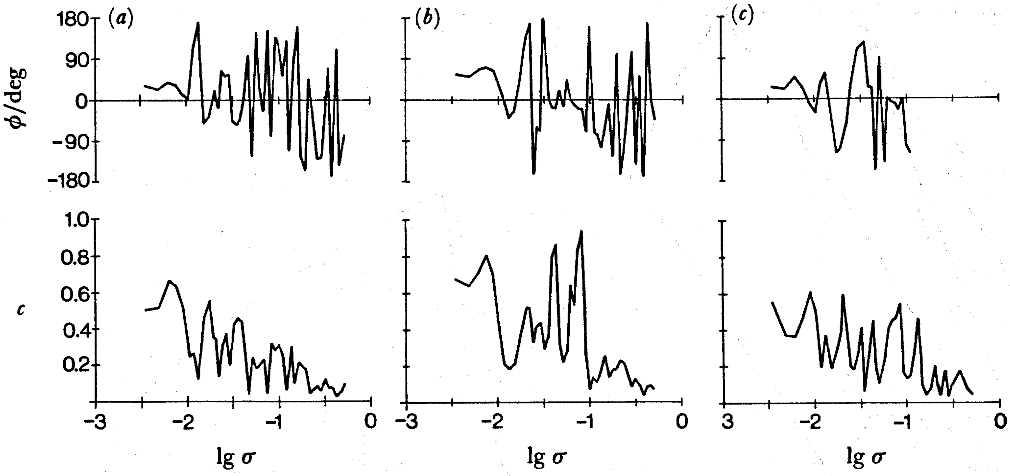

FIGURE 16. The phase, ϕ, and coherence, c, against lg σ (frequency, σ, measured in cycles h^{-1}) between (*a*) temperatures, (*b*) long-slope currents, and (*c*) x-slope currents at 30 m on mooring 373 and 281 m on mooring 375. Confidence limits are as in figure 14*a*.

The phase propagation between neighbouring instruments for the two periods that appear to have the most prominent baroclinic signals are summarized in figures 17 and 18. The sketches show the three moorings and their instruments, and numbers and arrows indicate phase differences and propagation directions. The 5.45 day period feature appears to propagate principally to the west, phase advancing polewards along-slope and off-slope. The mean long-slope wavelength determined from the means of phases when there is significant coherences (52.6°) is 61 km. The long-slope phase speed is thus about 13 cm s^{-1}, well in excess of the mean long-slope currents. The apparent off-slope wavelength is about 20 km. The general absence of notable vertical phase shifts at the upper instruments suggests barotropic motion but the low phase speed indicates that the motion is baroclinic. A downward phase motion seems to be prevalent in the lower part of mooring 375, whereas the off-slope wavelength is about 20 km.

At M_2 the phase propagation is predominantly towards the slope. At the upper instruments the phase propagation appears to be upwards (there is some doubt because of the large separation of the instruments and consequent uncertainty in establishing unequivocally the direction of phase advance). In temperature there is, however, a definite downward phase propagation in the lower instruments on mooring 373.

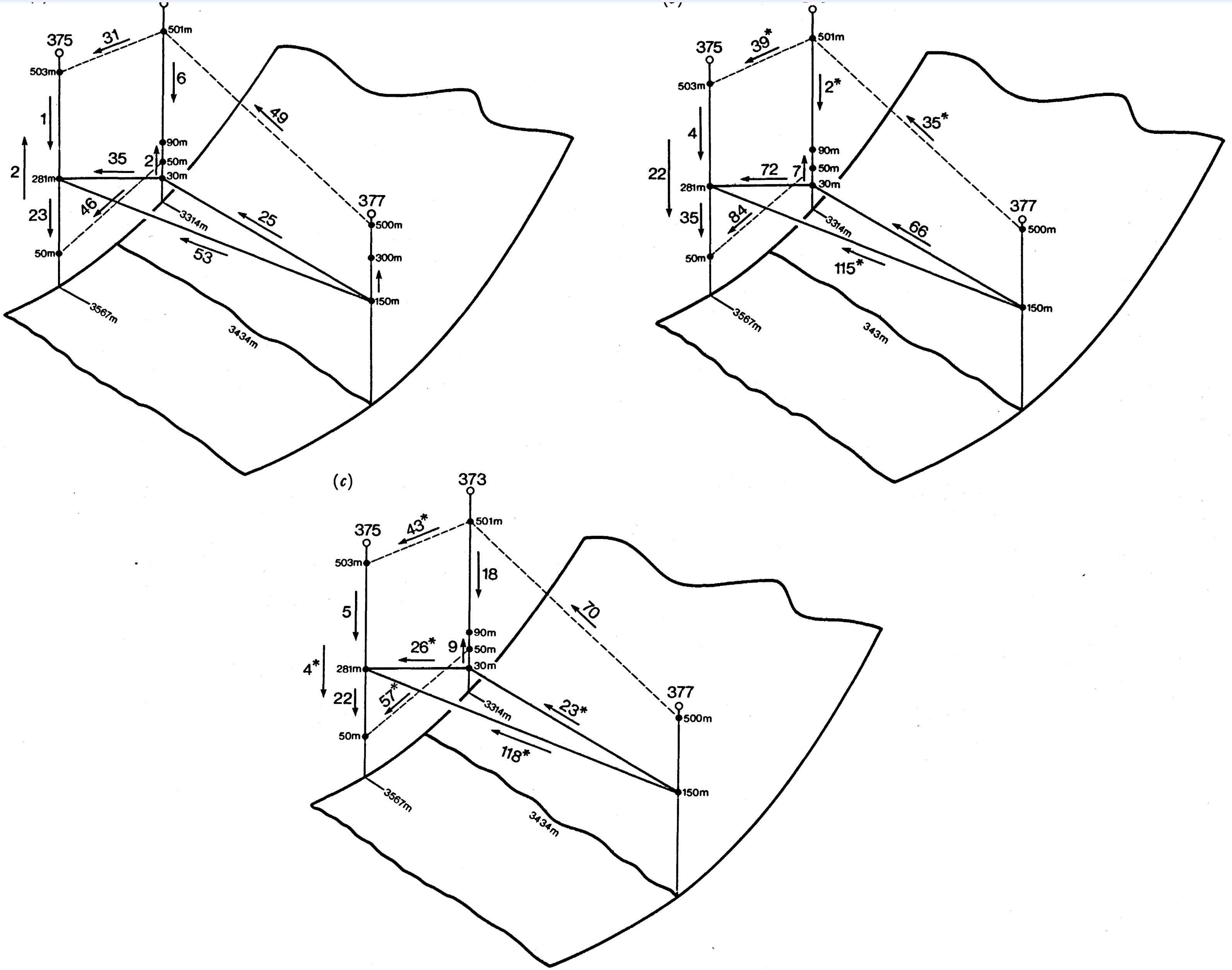

Figure 17. The phase differences and direction of phase propagation between instruments on the three moorings for 5.45 day periods. Phases marked with an asterisk are below the 95% confidence limits for coherences; (*a*) temperatures, (*b*) long-slope and (*c*) *x*-slope currents.

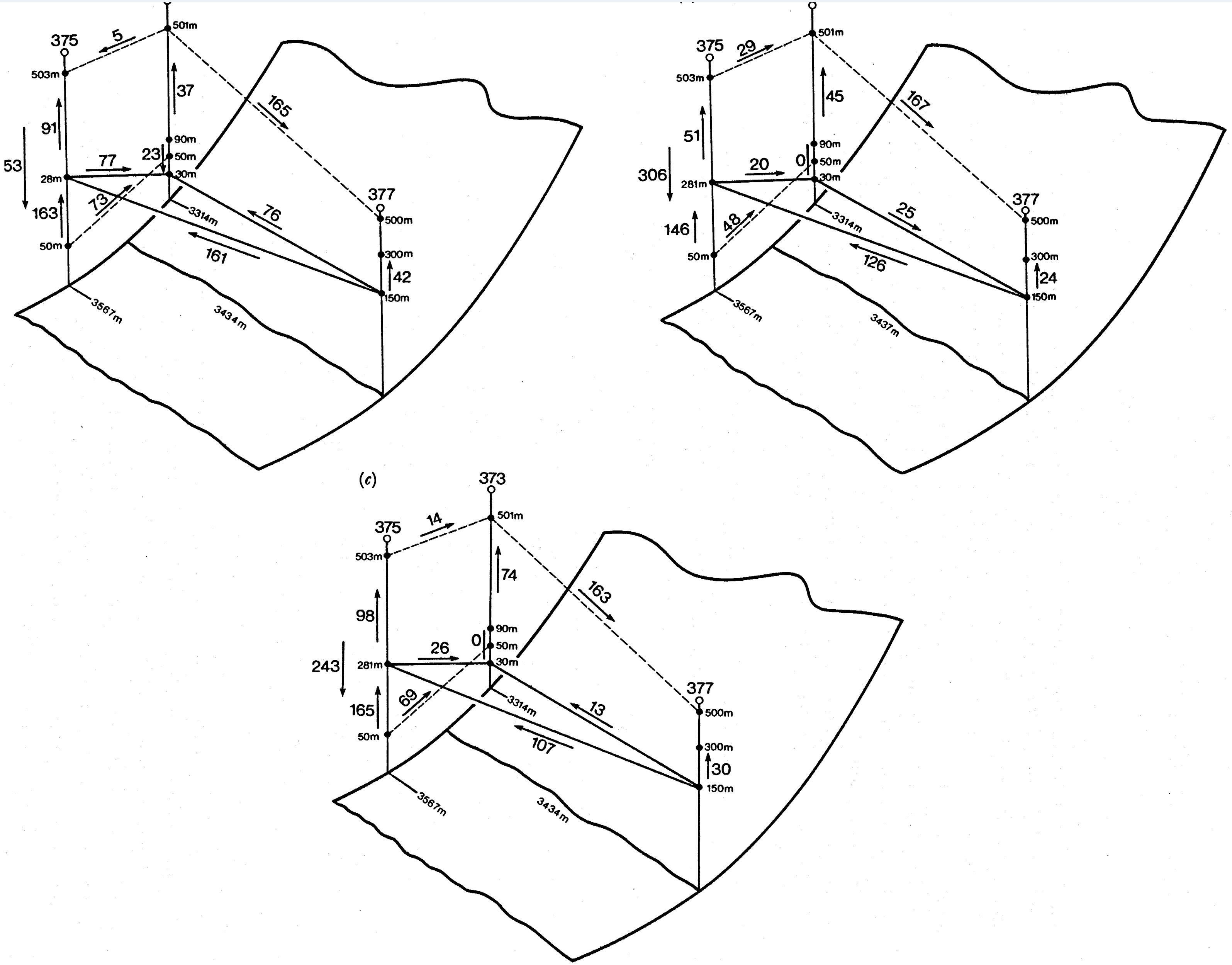

FIGURE 18. The phase differences and direction of phase propagation between instruments on the three moorings for M_2 tidal period, (*a*) temperatures, (*b*) long-slope and (*c*) *x*-slope currents.

4.4. *The advection of heat*

We have examined the terms

$$\frac{\partial T}{\partial t}+u\frac{\partial T}{\partial x}+v\frac{\partial T}{\partial y}$$

that appear in the diffusion–advection equation for temperature, taking average estimates over 1–8 tidal cycles of $\partial T/\partial t$ in the lower 90 m at mooring 373 and the long-slope temperature gradient from moorings 373 and 377 with the long-slope current, v, at 373. We supposed in addition that the component u is directed parallel to the local bottom slope, and derived the up-slope gradient, $\partial T/\partial x$, from the local vertical gradient between 30 and 90 m off the bottom and the x-slope gradient existing between mooring 373 and 375 but ignoring adiabatic changes. Table 2 shows the regressions between $\partial T/\partial t$ and $(u\partial T/\partial x+v\partial T/\partial y)$ and between $\partial T/\partial t$ and $u\partial T/\partial x$. The former are significantly negatively correlated with a slope near -1, showing that the temperature variation at a point responds primarily to advection and that the diffusive contribution to temperature is less important. Table 2*b* shows that, given the assumed averages, only about one quarter of the temperature variation results from the up-slope advection so that the temperature is responding primarily to the long-slope advection of temperature gradients. (The difference in spectral shape at low frequencies between the temperature and the x-slope current, figures 11 and 12, suggested that a simple explanation of temperature variation by movement of water up and down the slope is likely to be inadequate.) It is notable, however, that the scatter of points about the regressions is considerable; some account of diffusion appears necessary to explain this variability.

TABLE 2 (*a*). REGRESSION OF $y = \delta T$ WITH $x = \delta t[u\partial T/\partial x+v\partial T/\partial y]$

(The coefficients of the best fit curve $y = A+Bx$ and the regression coefficient are shown.)

averaging period/h	coefficients $\frac{A}{\text{K}}$	B	regression coefficient	10^2 deviation about regression/K
25	0.0126	−1.13	−0·41	3.9
50	0.0203	−1.01	−0.45	6.1
100	0.0497	−1.32	−0.33	9.3

TABLE 2 (*b*). AS IN (*a*) BUT WITH $x = \delta t[u\partial T/\partial x]$

averaging period/h	coefficients $\frac{A}{\text{K}}$	B	regression coefficient	10^2 deviation about regression/K
12.5	−0.0157	−4.16	−0.34	1·0
25	−0.0247	−3.34	−0.42	1.6
50	−0.0533	−3.63	−0.37	2.2
100	−0.1145	−3.81	−0.26	3.3

There are apparent x-slope and long-slope fluxes of heat; the mean values $F_u = \overline{(u-\bar{u})(T-\bar{T})}$ and $F_v = \overline{(v-\bar{v})(T-\bar{T})}$ are non-zero, where u is the x-slope current (in direction 040), v is the long-slope current and T is the temperature (all measured at a single instrument) and a bar represents a time average. The average values of F_u, F_v taken over all the instruments are -0.90×10^{-4} K m s^{-1} and -1.52×10^{-4} K m s^{-1}, respectively. The values of F_u are all of the same sign with $-1.84 \times 10^{-4} < F_u$ (K m s^{-1}) $< -0.02 \times 10^{-4}$, but with a consistent decrease towards the sea bed in the lower instruments at mooring 373. Values of F_v lie in the range $-4.45 \times 10^{-4} < F_v$(K m s^{-1}) $< 3.84 \times 10^{-4}$ with positive values at 10 m and with values less than -2.5×10^{-4} K m s^{-1} near 90, 300 and 500 m, the largest negative values being at 500 m.

These values suggest that these are net off-slope and equatorward long-slope fluxes of heat (or equivalently fluxes of density in the opposing directions) in the lower 500 m of the water column, and it is tempting to associate the former with an upwelling transport of colder water. It is possible however that the transports are not real, but a consequence of wave motions which lead to apparent fluxes. The u–T and v–T cospectra are dominated by components near M_2 frequencies. (The v–T spectra rise at very low frequencies, but the major contribution to the net power is at M_2.) We provide in Appendix A two simple examples that demonstrate the paradox that non-zero current and temperature correlations at fixed points in certain wave fields do not indicate a real transport of heat. The magnitude of the apparent wave-produced fluxes appear sufficient to explain those observed.

4.5. *Richardson numbers*

Figure 19 shows the histogram of the logarithmic gradient Richardson number Ri, estimated between 10 and 90 m on mooring 373. The mode is at $\lg Ri = 0.25$ showing that the flow on this scale is generally stable ($Ri > \frac{1}{4}$), judged by the Miles–Howard criteria (Miles 1961; Howard 1961).

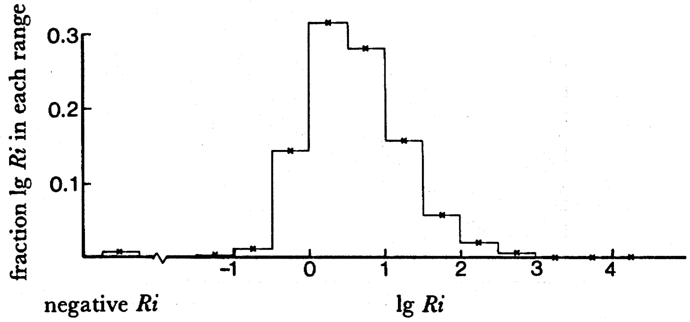

FIGURE 19. Histogram of lg *Ri* (gradient Richardson number) estimated from instruments at 10 m and 90 m on mooring 373.

5. TIDAL AND SHORT-TERM VARIABILITY

5.1. *Tidal variations*

The downward phase propagation at M_2 mentioned in §4.3 is also clear in figure 20, which shows the temperature and currents averaged over the semidiurnal tidal cycle. The peaks and troughs of temperatures and currents (figure 20*a*, *b*) lag successively as the distance from the sea bed decreases, indicative of downward phase propagation and a vertical wave-

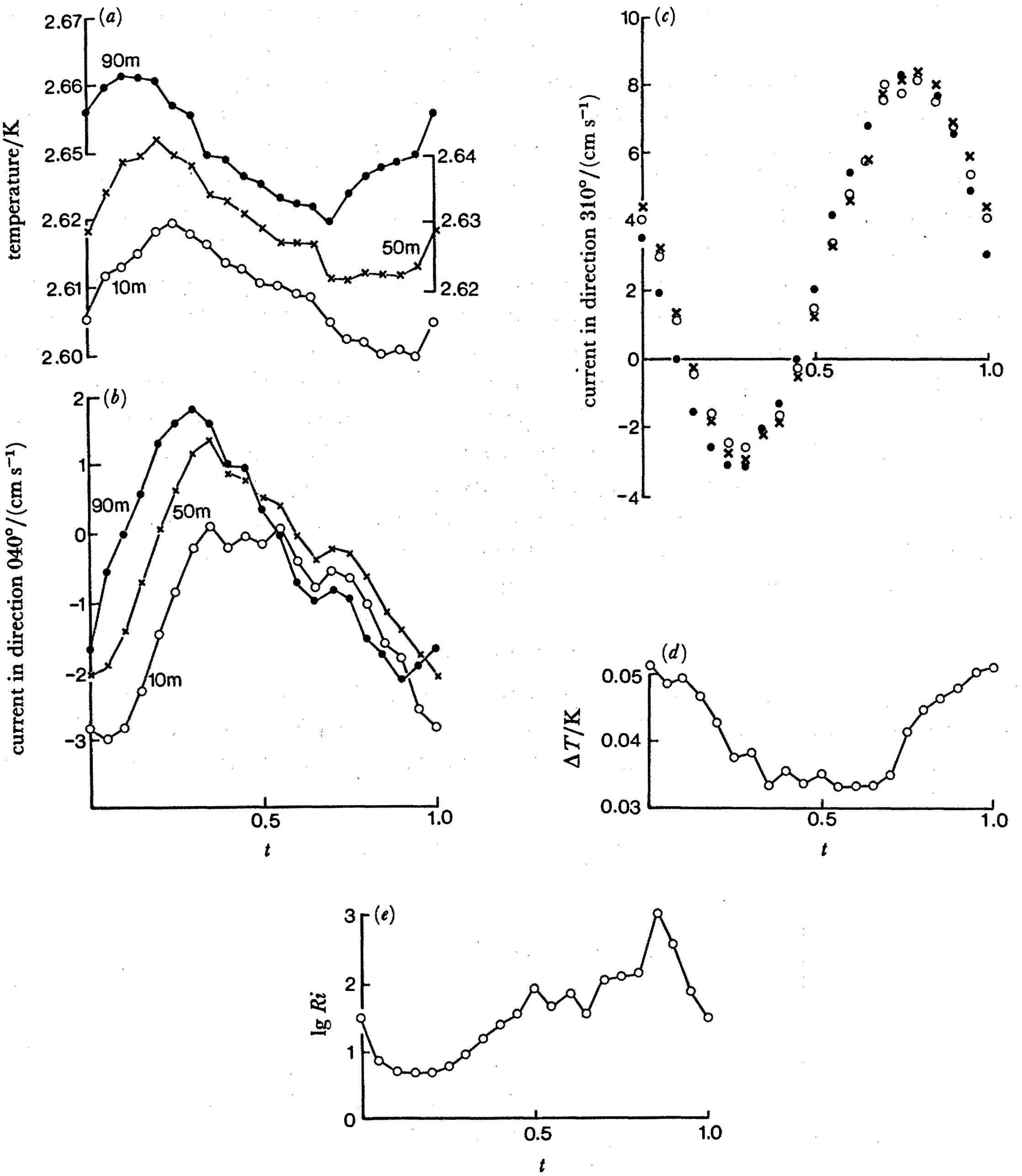

FIGURE 20. Variations over an M_2 tidal cycle at 10, 50 and 90 m of (*a*) temperture, (*b*) *x*-slope current, (*c*) long-slope current, (*d*) mean temperature difference between instruments 20 m apart and (*e*) Richardson number estimated by differences between 10 and 90 m at mooring 373. The time, *t*, represents the fraction of the M_2 tidal period. Averages were taken over 80 tidal cycles.

length of about 700 m. The amplitudes at the three levels 90, 50 and 10 m are similar for each respective component, but the long-slope current (figure 20*c*) has a much larger amplitude than the *x*-slope, and shows no indication of phase shift. Both temperature and *x*-slope current oscillations are asymmetrical, with relatively rapid rises in values. One important effect of the phase shift is to vary the current shear. It is much greater during the first half of the tidal cycle than in the second (figure 20*b*), the mean shear varying by ±100% from the mean value.

There is also a modulation of the temperature gradient by about 20% (figure 20*d*), the gradient being largest when the shear is greatest. In consequence, the mean Richardson number estimated between 10 and 90 m, with potential density calculated on the assumption that the mean *T–S* relation is fixed, varies as shown in figure 20*e*. The mean-gradient Richardson number reaches its minimum value as the temperatures are falling but in advance of the period when the overall gradient in temperatures is least.

5.2. *Observations with* BERTHA

The benthic resistance thermometer array consists of a chain of 11 platinum resistance thermometers sampling simultaneously every 10 s at 11 levels to a resolution of 0.1 mK. It is attached to a single wire mooring supported by a glass float buoyancy package. Relative intercalibration of the sensors is achieved by recording as the instrument free-falls to the sea bed and subsequently by adjusting the 11 recorded values to be, in a least mean squares sense, identical at each depth level at which temperature was recorded by a reference sensor near the centre of the vertical array. Values are then corrected to represent potential temperature by allowing for an appropriate adiabatic gradient. On recovery, the instrument is released acoustically from an anchor weight at the lower end. The instrument was deployed for a period of 26.5 h in May 1985 some 60 m (determined acoustically) from mooring 373, with sensors every 10 m from 10 to 90 m and at 110 and 130 m.

Figure 21 shows the potential temperature variations measured at the 11 sensor levels for the whole deployment period. Several features are immediately obvious. There is a wave-like variation with an apparent period near 13 h. The phase of the variation differs by about 1.5 h over the 120 m vertical range of the array, the maxima and minima being reached earlier at the uppermost sensors. The effective vertical wavelength is about 1000 m, somewhat larger

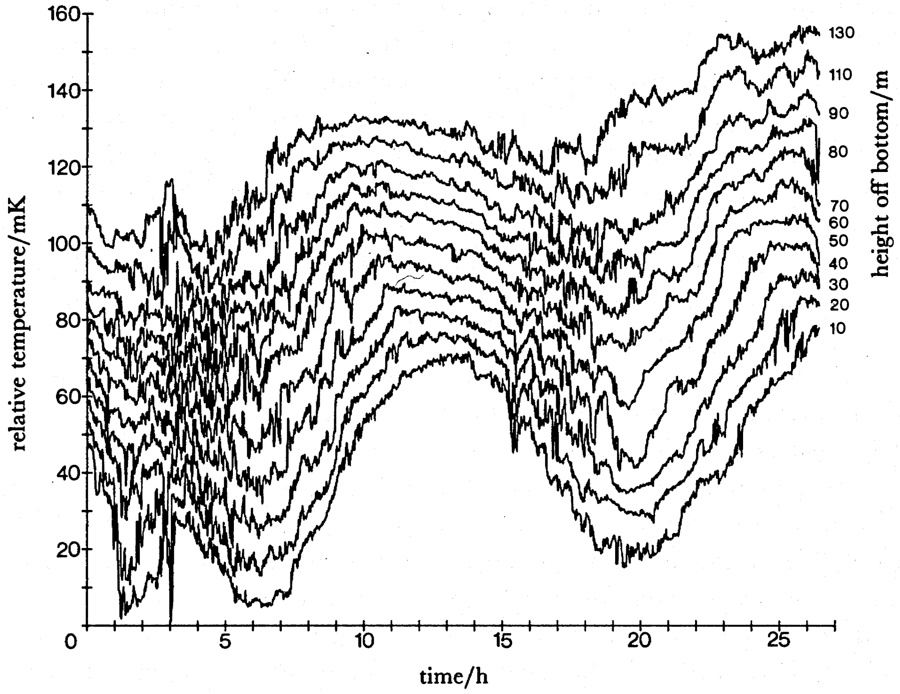

FIGURE 21. Variations in potential temperature with time. Each record is off set by 5 mK. The sensor heights above the bottom (in metres) are shown at the right.

than found for the M_2 baroclinic tide in §5.1. The amplitude of the temperature variation decreases with height off the bottom. There is evidence of more intense fluctuations when the temperature at the lower sensors is falling than at other times. Generally the short-period (less than 1 h) variations lack coherence between neighbouring sensors.

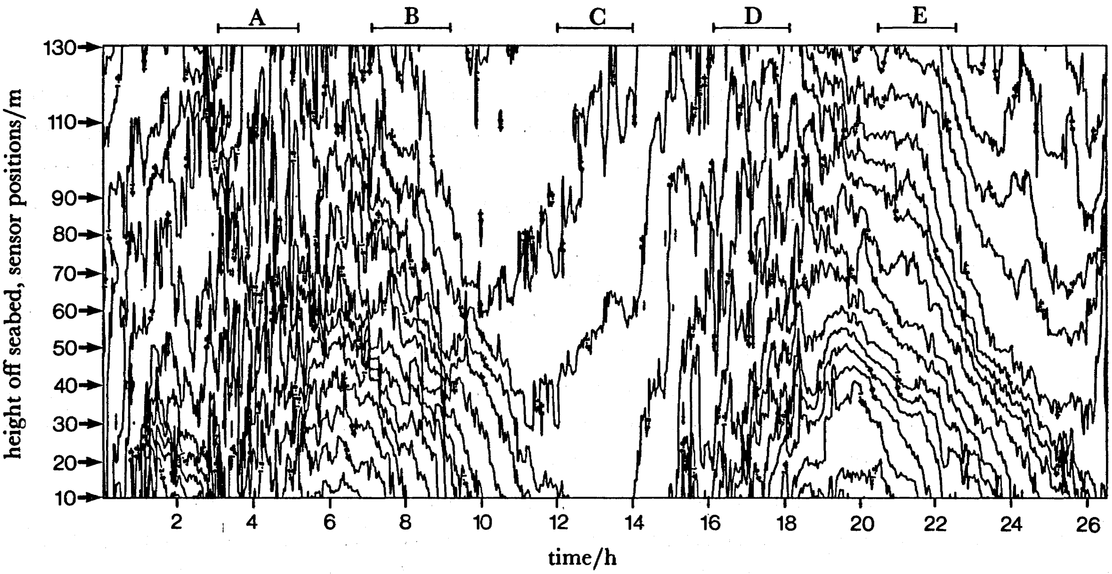

FIGURE 22. Variation of potential isotherm level with time. Points are 2 min intervals are plotted with 5 mK separation between contours.

These features are also seen in the contours of potential temperature (figure 22), but in addition there are others. When the isotherms near the sea bed reach their maximum height, colder water is found near the bottom than is present at other times; processes of horizontal (or up-slope) advection appear important. The contours cross both the 10 and 130 m levels so that the height of the 'waves' exceeds the 120 m sampling range. The top:bottom vertical gradient of potential temperature changes during the record by a factor of about 8:1, larger than the average variation observed in the current meter records (§5.1 and figure 20*d*). The lowest gradients, about 0.1 mK m^{-1}, are when the temperature at 10 m is greatest, that is at the wave trough. The overall structure is similar to that of internal tidal waves (or tidal bores) observed by Cairns (1967) in much shallower water.

There is no evidence of a sustained well-mixed boundary layer adjacent to the sea bed, and if such layers are present they must be less than 20 m in vertical extent. There are, however, temperature inversions in which the potential temperature increases with depth. We have selected for closer examination five periods of 2 h (A–E in figure 22) that characterize the variations seen in the total record. Contours, all at the same contour interval (2 mK), are shown in figure 23 (*a–e*). A and D are periods of considerable thermal activity and generally rising isotherms. The mean current during A is much larger than at D (see figure caption), but in each there is an up-slope component and in overall structure the two records, 13 h apart, are remarkably similar. Although the mean vertical gradients (see figure 22) are relatively large, inversions in the gradient will later be shown to be fairly common. The records are marked by regions where four or five of the contours cluster together for periods of typically

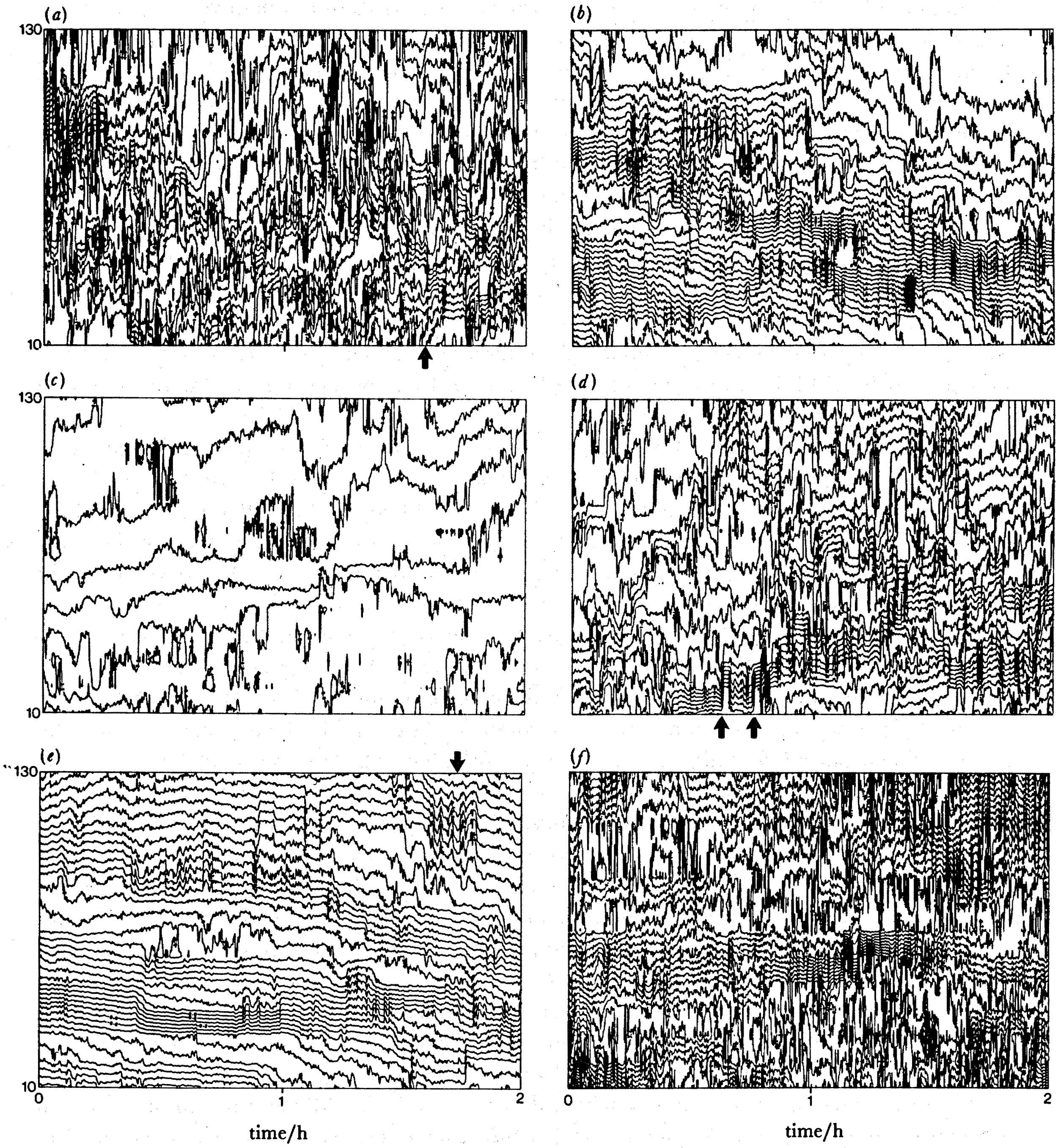

FIGURE 23. (*a*)–(*e*) Show two-hour long isotherm contour plots at times A–E shown in figure 22. The contour interval is 2 mK. (*f*) The period C contoured at 0.5 mK. The mean flow conditions are measured by instruments between 30 and 90 m on mooring 373 and are as follows.

period	potential temperature gradient mK m^{-1}	current speed cm s^{-1}	current direction deg	mean Richardson number, *Ri*
A	0.27	9.47	316	1.83
B	0.55	3.61	244	1.52
C	0.081	3.61	333	0.81
D	0.29	4.51	317	1.19

(Mooring 373 was recovered before period E.) The mean Richardson number is estimated over 60 m between 30 and 90 m.

40 min, occasionally jumping suddenly upwards or downwards in less than 20 s (e.g. at 40 m, above the arrow in A and at 20 m, above the arrows, in D), but generally appearing to fall in level, contrary to the general trend in isotherms and suggesting an association with upward propagating internal waves (Lazier 1973). If, as is likely, these layers are advected by the ocean current, their horizontal scale must be of the order of 200 m. The intensity of the large vertical gradients is inadequately resolved by the contouring; the abrupt jumps appear as the regions of high gradient ('sheets'), apparently less than 1 m in thickness, move past the level of a sensor. The layers are also seen at other times (i.e. in B, D, E and F) and are vertically separated by typically 20–60 m. Fluctuations in isotherms of periods of about 5 min can be seen with amplitude of about 5 m. This period is far less than the mean buoyancy period, $2\pi/N$, of about 2.5 h. Local gradients would have to be increased by factors of about 870 to allow internal waves of 5 min period to occur. Doppler-shifted internal waves may be present but to have this period must be of horizontal scale of only 10–20 m or less, and perhaps it is more likely that the fluctuations are due to turbulence.

The periods B and E are of falling isotherms, low currents with off-slope components, very much less activity and more persistent layers. The general absence of abrupt jumps in the position of the layers suggests that, although the potential temperature differences across them are similar, they are broader than in A and D (perhaps 5–10 m). Occasional bursts of high frequency (1–2 min period) fluctuations can be seen (e.g. at 110 m below the arrow in E), but inversions over the 10 m separation of the sensors are very rare.

Period C contrasts sharply with the others. The mean gradients (figure 22) are very weak, and currents are low but have an up-slope component. Overall, the upper isotherms are rising, but the lower are almost steady. The overall Richardson number is low, falling to 0.25 at the end of the period and inversions are fairly common, but regular fluctuations are virtually absent. When contoured at higher resolution (0.5 mK, figure 23*f*) we see that there are layers persisting for at least 1 h although with frequent inversions in the weaker gradients.

The spectra of the temperature fluctuations in the periods A to D, ensemble averaged over the sensors, are shown in figure 13. The spectral level varies by about an order of magnitude between periods A and C. The spectral slope is near $-\frac{5}{3}$, as might be expected in turbulent motion in an inertial-convective range at frequencies exceeding the mean value of N (Monin & Ozmidov 1985), and the points appear approximately to form a continuation of the trend apparent in the spectra from the instruments of mooring 373. When scaled with potential temperature gradients to give equivalent vertical-displacement spectra, the spectral levels in periods A, C, and D are approximately equal, but that of period B is one decade lower.

Figure 24 shows the mean percentage of the record containing temperature inversions in each hour as functions of time and of height above the sea bed. Although the sensor resolution is about 0.1 mK there is little confidence that differences between sensors are determined to greater accuracy than 0.5 mK by the calibration method. (The smoothness of the mean profiles provides a test of this accuracy.) We have therefore chosen to 'recognize' an inversion only if the temperature difference between an upper and lower sensor is less than −0.5 mK. The greatest number of inversions occur when the mean gradient is least, near the beginning of, and 13.5 h into, the record. The large percentage persists during the active periods when the isotherms are rising (figure 23*a*, *d*). There are, however, very few inversions when the isotherms are falling. There is evidence of a rise in the percentage of inversions at the lowest sampled levels, 10–20 m, and also above 60 m, with an apparent peak near 80 m.

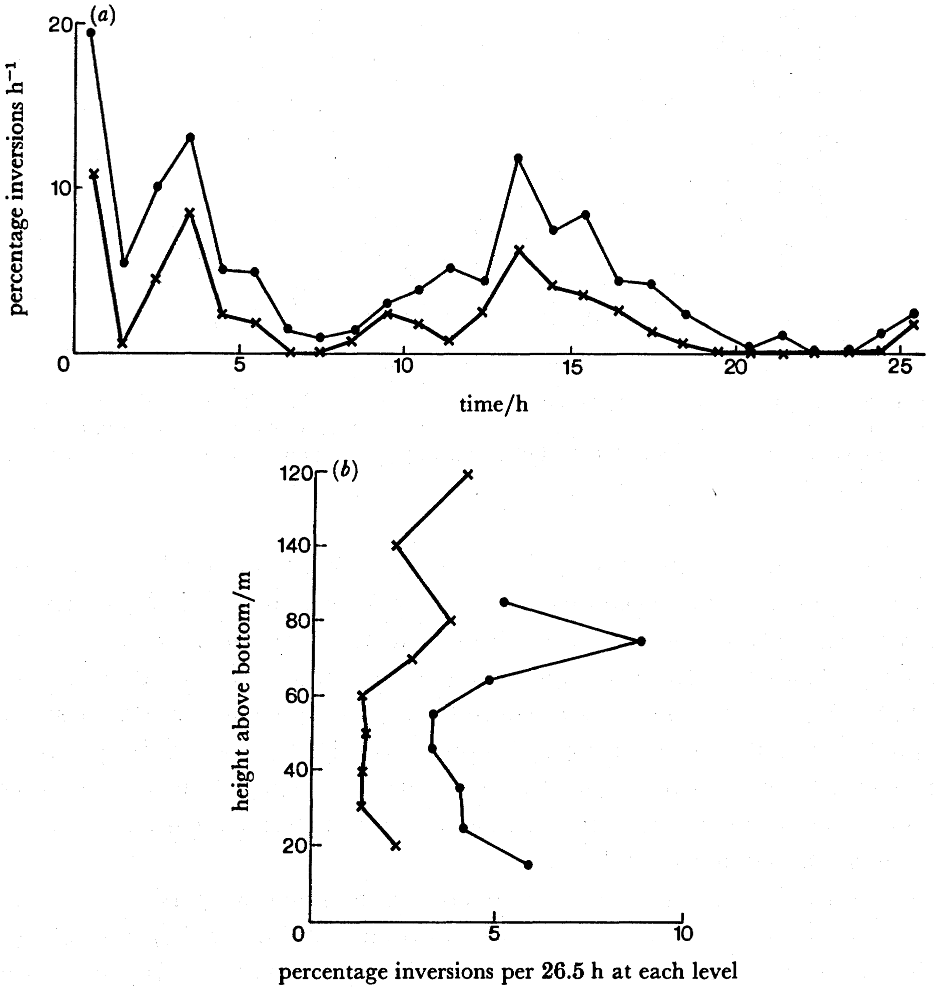

Figure 24. (*a*) The percentage of inversions in each hour as a function of time. Dots represent inversions extending over 10 m (360 records each hour from each of 8 pairs of sensors between 10 and 90 m) and crosses those over 20 m (360 records each hour from each of 7 pairs of sensors between 10 and 130 m). (*b*) The percentage of inversions as a function of height above the bottom for the whole record, dots over 10 m separation, crosses over 20 m separation.

5.3. *The scale and persistence of inversions*

We have compared the observed scale of inversions found in the CTD records (§2.2) with those measured by BERTHA, again recognizing an inversion only if the potential temperature difference was less than some 'noise' level. Here two levels were selected, −0.5 mK and −1.0 mK. Figure 25 shows the percentage of inversions observed at each scale as a function of the vertical separation. There is fair agreement for the 10 and 20 m separations, but the BERTHA measurements exceed the frequency of CTD inversions occurring over 30 m.

The data sets are not fully comparable. At 30 m separation the CTD estimate is based on 762 observations in 7 casts made in different positions over two weeks. The estimates from BERTHA are based on 65520 observations made at one site every 10 s over 26.5 h. The inversions in the CTD record, especially the largest, were not adequately sampled. The estimates from BERTHA are based on simultaneous measurements at two sensors, one vertically above the other; the CTD

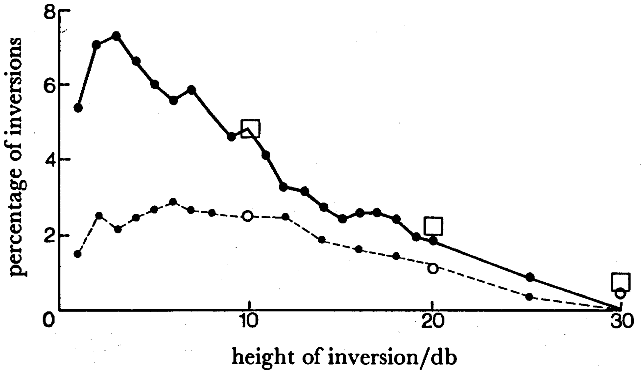

Figure 25. The percentage of inversions in potential temperature measured at different vertical separations on (full and broken curve) CTD casts and (squares and circles) from BERTHA. Only temperature differences less than -0.5 mK are recognized as inversions for the full curve and squares; only less than -1.0 mK for the broken curve and circles.

estimates are based on samples at time intervals dependent on the lowering rate of the instrument and at positions that, because of ship drift, currents, or shear, may be some distance apart. The two CTD casts having very large displacements were discarded from analyses, but their inclusion would have produced much higher percentage values than are shown in figure 25. Although at these large scales the samples are not sufficient for reliable statistics, the large inversion found in the CTD record are also present in that of BERTHA. It appears plausible that the inversions leading to the large displacements (e.g. figure 6) in the CTD profiles are because of the same events as cause the inversions in the BERTHA record and that both are associated with the baroclinic M_2 tide.

We have examined the BERTHA records to determine the apparent persistence of inversions, that is to examine the 'runs' (as the term is used in probability theory) of unstable gradients. Figure 26 shows the fraction of the total number of inversions that 'persist' for times, T. We have taken 10 m separations and two 'noise' levels. There is little to choose between them although, as the absolute value of the noise level increases, the number of samples decreases. The proportion of runs decreases as T increases. The average 'run' length is about 27 s; 10% of the runs persist for times in excess of 60 s. There are insufficient data to establish whether the persistence of inversions depends on height above the sea bed or on their amplitude. The persistence time is comparable to the time required to lower the CTD through distances equal to those between the larger BERTHA sensor separations examined in figure 25. We therefore reanalysed the BERTHA data to provide a measure of inversion frequency that can be compared with the CTD data by finding the frequency of inversions between sensors separated vertically by 10, 20 and 30 m, but at time delays of 10, 20 and 30 s respectively to simulate the delay in sampling at these separations as the CTD is lowered (at about 1 m s^{-1}; this, however, supposes that the CTD is not moving laterally as it is lowered). The results did not differ significantly from those presented in figure 25).

Observations at all 11 temperature sensors were made every 10 s. It is thus not known whether the inversions have really persisted in time between successive observations or whether, by chance, one is succeeded by others, each being short lived and happening to occur when sampling took place. Making the hypothesis that the latter occurs and that short-lived inversions occur with probability p, then, provided the number of observations is sufficiently large (our sample exceeds 6×10^4), the probability of an inversion is given by the number of inversions divided by the number of samples (e.g. $p = 0.047$ for 10 m sensor separation at 0.5 mK noise). Having recorded a run of n inversions, the chance that the next will be an inversion is p. Hence if I_n is the probability of a run of length n, $I_{n+1} = pI_n$, and, normalizing the sum, ΣI_n, to unity we have $I_n = p^{n-1}(1-p)$. The average run length is $1/(1-p)$. Comparing these estimates with observations (figure 26) we find that

(*a*) the observed value of the average run length is much in excess of that predicted; and

(*b*) except at $n = 1$ (time = 10 s), the run lengths observed exceed that predicted.

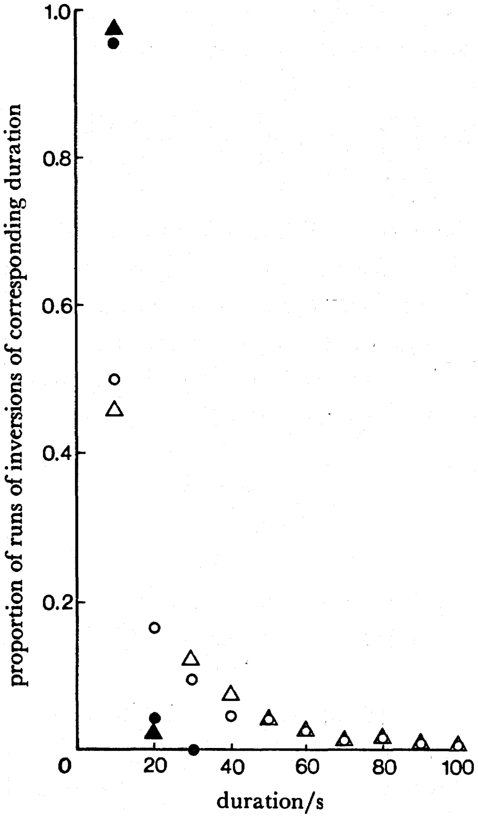

FIGURE 26. The persistence of inversions in potential temperature between sensors separated vertically by 10 m. The open symbols represent observations and the closed symbols are theoretical predictions based on an assumption of the random occurrence of inversions (see 3.3). Circles: inversion threshold – 0.5 mK. Triangles: inversion threshold – 1.0 mK.

These conclusions support the rejection of the hypothesis that the runs are caused by the random sequential occurrence of short-lived inversions. The frequency of inversions is, however, not stationary in the overall record (as figure 6*a* shows), and further consideration is required to determine the true nature of runs. Nevertheless we emphasize the main conclusion: the persistence of large scale (greater than 10 m) inversions appears to be rather short, much less than the time scale N^{-1} (about 0.35 h). Given a typical current of 4 cm s^{-1} (caption to figure 23) the apparent horizontal scale of the 'average inversion' extending to 10 m is about 1.1 m and the largest exceed 4 m.

5.4. *Small-scale mixing and diffusion by salt fingers*

We have found evidence of high frequency variability (figure 21) and inversions (figure 24) associated with the fluctuations of about tidal period. Comparing figures 20, 21 and 24, we see that the inversions appear most frequently at about the time when the temperature at 10 m reaches a maximum, and shortly after the overall Richardson number is low. This suggests that a shear-flow Kelvin–Helmholtz instability resulting from flows associated with the baroclinic M_2 tides may be the cause, the lag being necessary for instabilities to grow.

We shall consider the diffusion accompanying the inversions in §5.5, and the processes leading to the onset of instability in §6. It is, however, conceivable that double diffusive salt-finger convection might also contribute significantly to diffusion.

The maximum growth rate of the fingers, λ, may be obtained from the expression

$$\lambda = \left(\frac{\kappa}{\nu}\right)^{\frac{1}{2}} (g\alpha_1\, T_z)^{\frac{1}{2}} \left[1 - \left(1 - \frac{1}{R_\rho}\right)^{\frac{1}{2}}\right], \tag{7}$$

by using the Stern (1975) and Schmidt & Evans (1978) formulation, where κ is the thermal diffusivity, ν is the kinematic viscosity and T_z in the vertical temperature gradient. The calculated e-folding times, λ^{-1}, vary from 2.6 to 6.6 h during the period of the BERTHA deployment and are, on average, about 2.4 h for the 8 month current meter deployment. (We have used $\kappa = 1.4 \times 10^{-7}\ \mathrm{m^2\,s^{-1}}$, $\nu = 1.3 \times 10^{-6}\ \mathrm{m^2\,s^{-1}}$.) This seems barely sufficient to establish convection during the M_2 cycle. The width of the fingers,

$$L = \pi \left(\frac{4\nu\kappa}{g\alpha_1\, T_z}\right)^{\frac{1}{4}} \tag{8}$$

(Stern 1960) is 6.5 cm or, from the finite amplitude maximum growth and equilibrium estimates of Schmidt (1979), 3.1 and 2.6 cm respectively, below the scales detectable by the instrumentation.

The layers of thickness 1 m of large temperature gradient seen in the BERTHA record (§5.2) are consistent with layers of salt fingers roughly 15 times their wavelength (see Gargett & Schmidt 1982) between the relatively uniform convectively mixed regions, observed to be of order 20 m in thickness. We may devise an estimate of the density flux due to the salt flux in salt-finger convection, βF_s, from McDougall & Taylor's (1984) empirical results. At $R_\rho = 2.44$ they find $\beta F_s = 0.12\ (g\kappa)^{\frac{1}{3}}\ (\alpha_1 \Delta T/R_\rho)^{\frac{4}{3}}$ (see their figure 3) and the ratio, $\alpha_1 F_T/\beta F_s$, of contributions of heat and salinity to the buoyancy flux, $R_f = 0.43 \pm 0.1$ (see their figure 4). Recalling that the vertical gradients in the $h = 1$ m thick layers are some 20 times the average so that $\Delta T = 20 h T_z$, we can estimate the heat flux

$$\alpha_1 F_T = R_f \beta F_s = 0.12 R_f (g\kappa)^{\frac{1}{3}} (\alpha \Delta T/R_\rho)^{\frac{4}{3}},$$

and compare it with $K_v \alpha_1\, T_z$ due to a vertical diffusion coefficient of heat K_v in the mean temperature profile in the near bottom layer derived from observations (§5.5). The ratio is $3.5 \times 10^{-5} K_v^{-1}\ (\mathrm{m^2\,s^{-1}})$ so that double diffusive convection is only likely to make an important contribution to the heat flux if the estimated value of K_v is about $10^{-4}\ \mathrm{m^2\,s^{-1}}$ or less.

5.5. *Turbulence in the boundary layer: an estimate of K_v and the production of turbulent kinetic energy*

An estimate of the rate of turbulent kinetic energy per unit mass, ϵ, may be found by assuming that the displacement scale d, is proportional to the Ozmidov length scale (Thorpe 1977);

$$d = c_1 \epsilon^{\frac{1}{2}} N^{-\frac{3}{2}}, \tag{9}$$

where the constant of proportionality, c_1, has been determined empirically by Dillon (1982) and Crawford (1986) as about 1.25. If further we use the relation $K_v = \gamma \epsilon N^{-2}$ proposed by Osborn (1980) and the mean value of $\gamma = 0.24$ from estimates of Oakey (1982, 1985) and Gregg *et al.* (1986) we have

$$K_v = 0.15 d^2 N. \tag{10}$$

In §2.2 we found estimates of $d = 6.5$ and 15.1 m that, from the mean value $N = 7.1 \times 10^{-4}$ s^{-1}, give $K_v = 4.5 \times 10^{-3}$ and 2.4×10^{-2} $\mathrm{m^2\,s^{-1}}$. These values are so large that it is unlikely that double diffusive convection is a dominant process in mixing (see §5.4).

The rate of production of turbulent kinetic energy per unit area, P_1, to support the estimated dissipation in a height h of the water column above the sea bed (e.g. that in which α is measured) may be estimated. If ϵ, given by (9), is the result of Kelvin–Helmholtz instability associated with the tidal inversions (as suggested earlier) then $P_1 = c_2 h \epsilon$, where c_2 is a constant that has values in the range 1–1.33 depending on the Richardson number at which instability occurs (Thorpe 1973). At marginal instability, when the Richardson number is close to critical, it appears that $c_2 \sim 1$. We shall take this value here although some doubt exists over the appropriate value. The lower value underestimates P_1. The mean rate of production at the sea bed through the working of the stress is $P_2 = C_D \overline{U^3}$ where U is the current near the sea bed and C_D is the drag coefficient. Using $C_D = 3 \times 10^{-3}$ (Heathershaw 1979), $(\overline{U^3})^{\frac{1}{3}} = 8.2$ $\mathrm{cm\,s^{-1}}$, $h = 150$ m, $N = 7.1 \times 10^{-4}$ $\mathrm{s^{-1}}$ and the estimates $d = 6.5$ and 15.1 m, we find values for the ratio

$$R = \frac{P_1}{P_2} = \frac{c_2 h d^2 N^3}{c_1^2 C_D \overline{U^3}}$$

of 0.9 and 4.7. Within this layer as much turbulent kinetic energy may be produced by the tidal-period inversions as by the bottom stress, and probably more. It thus seems likely that the energy supplied to the inversions cannot be derived solely from that produced by the working of the bottom stress on the sea bed (which is likely to be dissipated close to the bottom and is unlikely to produce inversions far above; see §3.3) and that an alternative source, the internal tides, provides the energy to sustain the inversions. A consequence is that, although a scaling law for turbulence depending on distance from the bed will, as usual, be appropriate close to the boundary, the turbulence in the body of the layer will be characterized by a scale determined by the processes leading to the tidal inversions. The dependence of ϵ with height z will, in particular, be determined by the processes leading to the instabilities. (For example in studies of two-dimensional internal waves, we have shown (Thorpe 1987) that the distance from a reflecting boundary at which the waves may break is dependent on three parameters, the bottom slope, the inclination of the group velocity vector to the horizontal and the wave steepness. The boundary layer structure in such a wave field will depend on these parameters.)

We now consider the implication of such a slope boundary layer for stability in the presence of long-slope flows.

6. THE STATIC STABILITY OF A BOUNDARY-LAYER FLOW ON A SLOPE

6.1. *Steady flows*

Long-slope flows tend to drive up- and down-slope currents in the Ekman-like boundary layer. These, given sufficient forcing, can lead to less dense water being driven down-slope under denser fluid, or conversely dense fluid up-slope over lighter fluid (Weatherly & Martin 1978) and so to conditions of static instability unless diffusion is sufficient to compensate. Instability of this nature has recently been studied by Smeed (1986) in laboratory experiments. We propose here an analytical model of a boundary layer on a slope (in contrast to the numerical models of Weatherley & Martin (1978)) to describe the conditions in which static instability is first attained.

In 1970, Wunsch and Phillips independently proposed steady solutions that describe the mean flow in a Boussinesq fluid of constant viscosity ν and diffusivity κ in which the mean density gradient is constant far from a uniform slope inclined at angle α to the horizontal. Wunsch included the effects of rotation and Phillips pointed out that exact solutions of the fully nonlinear equations of motion can be found. Motion is driven by the necessity for the density gradient normal to the slope to vanish, so satisfying the condition that the flux through the slope is zero. Isopycnal surfaces are thus inclined to the horizontal in the vicinity of the slope and this results in a horizontal pressure gradient that drives the flow.

If we take (x, y, z), $(u, v, 0)$ as coordinates and velocity respectively up, along, and normal to the slope and $\rho = \rho_0(1-\beta(z\cos\alpha + x\sin\alpha)+\gamma(z))$ so that the vertical density gradient tends to a constant value, $-\beta\rho_0$, if $\gamma(z)$ tends to zero far from the slope, and there is no along-slope density gradient, then Phillips's exact solution (here adding the effects of rotation) is

$$u = 2\kappa q \cot\alpha\, \mathrm{e}^{-qz} \sin qz \tag{12}$$

$$v = -\frac{f_1 \kappa}{\nu q} \cot\alpha (1-\mathrm{e}^{-qz}\cos qz) \tag{13}$$

$$\gamma = -\frac{\beta\cos\alpha}{q}\,\mathrm{e}^{-qz}\cos qz, \tag{14}$$

where $f_1 = f\cos\alpha = 2\Omega$, where Ω is the component of the Earth's rotation normal to the slope, $N^2 = \beta g$, and

$$q^4 = \frac{1}{4}\left(\frac{N^2\sin^2\alpha}{\nu\kappa} + \frac{f_1^2}{\nu^2}\right). \tag{15}$$

This solution satisfies the boundary conditions $u = v = \kappa\,\partial\rho/\partial z = 0$ at $z = 0$† and u, γ tend to zero at infinity. The upslope variation of u, v and γ is zero, and $u > 0$ for small distances z from the slope. The vertical density gradient, $\rho_0(\cos\alpha\,\partial\gamma/\partial z - \beta)$ is never positive and therefore the flow is statically stable. This solution has a prescribed value of v at infinity, $v(\infty) = -f_1\kappa\cot\alpha/\nu q$, in negative y-direction. There is no flexibility in the choice of $v(\infty)$; the 'interior flow' is set by the boundary conditions.

A model that more closely resembles the oceanic situation is, however, one with relatively large values of κ and ν near the boundary and small values far away. Neglecting rotation, this

---

† The no-slip condition may be replaced by a more realistic condition (e.g. by using a quadratic representation for the stress $\nu\,\partial u/\partial z = C_D(u^2+v^2)^{\frac{1}{2}}u$, $\nu\,\partial v/\partial z = C_D(u^2+v^2)^{\frac{1}{2}}v$) but for simplicity this is not presented here.

can be simulated in a laboratory experiment in which a grid of horizontal bars resting on an inclined plane in a stratified fluid is rapidly oscillated to produce turbulence. Unlike the horizontal grid mixing experiments (see, for example, Turner 1973, ch. 9) this produces mean flows that are directed up and down the slope (see Thorpe 1982, §1; Phillips *et al.* 1986).

Suppose now that $\nu = \nu(z)$, $\kappa = \kappa(z)$ and ρ is as before. Then, even in a rotating fluid, it follows from conservation of density in a steady flow that because

$$u\frac{\partial \rho}{\partial x} = \frac{\partial}{\partial z}\kappa\frac{\partial \rho}{\partial z}, \tag{16}$$

where $u(z)$ is the up-slope flow,

$$\begin{aligned}\int u\,\mathrm{d}z &= -\frac{1}{\beta\rho_0\sin\alpha}\left[\kappa\frac{\partial\rho}{\partial z}\right]_0^\infty \\ &= \kappa(\infty)\cot\alpha\end{aligned} \tag{17}$$

because there is no flux through the slope at $z = 0$. The net volume flux up the slope is independent of the intensity of mixing as measured by the magnitude of κ or ν near the boundary.

A simple model to take is the two-layer,

$$\nu, \kappa = \begin{cases}\nu_1, \kappa_1, & 0 < z < h \\ \nu_2, \kappa_2, & z > h,\end{cases} \tag{18}$$

with boundary conditions u, v, $\kappa\partial\rho/\partial z$, $\nu\partial u/\partial z$, $\nu\partial v/\partial z$ $\partial p/\partial x$ continuous at $z = h$, where $\partial p/\partial x$ is the up-slope pressure gradient; we assume $\partial p/\partial y = 0$. The problem is underspecified. The general solution in each layer

$$u = -\frac{2q^2\kappa}{\beta\sin\alpha}[\mathrm{e}^{-qz}(b\sin qz - a\cos qz) + \mathrm{e}^{qz}(c\cos qz + d\sin qz)] \tag{19}$$

$$v = -\frac{f_1\kappa\gamma}{\nu\beta\sin\alpha} + c_1 z + c_2, \tag{20}$$

with $$\gamma = \mathrm{e}^{-qz}(a\sin qz + b\cos qz) + \mathrm{e}^{qz}(c\sin qz + d\cos qz) + \frac{\beta\sin\alpha}{4q^4\kappa\nu}(c_0 + f_1 c_1 z + f_1 c_2), \tag{21}$$

has too many unknown constants (a, b, c, d, c_0, c_1, c_2), and one additional condition must be specified. Perhaps the simplest is that (a) ρ is continuous at $z = h$; in this case $v(\infty)$ is prescribed as in the Phillips–Wunsch solution. An alternative is to take (b) $v(\infty) = 0$; this results in general in a discontinuity in ρ at $z = h$ and in the appearance of positive, statically unstable, density gradients. (The equivalent of the familiar Margules relation at $z = h$ is

$$[v] = \frac{g\sin\alpha}{\rho_0 f_1}[\rho] - \frac{\nu}{f}[u''],$$

where the gradient of the upslope shear, u'', can no longer be neglected.) We may, however, find the range of values of $v(\infty)$ for which a statically stable density gradient may be obtained.

We illustrate these solutions by selecting values $N = 10^{-3}\ \mathrm{s^{-1}}$, $f_1 = 10^{-4}\ \mathrm{s^{-1}}$, $h = 50$ m, $g = 9.8\ \mathrm{m\ s^{-1}}$ and $\nu_1 = \kappa_1 = 10^{-2}\ \mathrm{m^2\ s^{-1}}$ that, roughly, fit the observations. We have chosen for simplicity also to take $\nu_2 = \kappa_2 = \kappa$.

Figure 27 shows $v(\infty)$ found for case A at various values of κ and slope angles of 5 and 10°. In contrast to the Phillips–Wunsch solution, positive value of $v(\infty)$, corresponding to the observed mean northwestward flows, are found for values of κ_1 sufficiently less than κ, the diffusivity in the exterior flow. Figure 28 illustrates the solution for u, v and ρ. These have relatively uniform lower layers that are either capped with a rapid change in ρ when $v(\infty) > 0$ at small κ (figure 28*a*), or relatively small changes in the variables when κ approaches κ_1, the Phillips–Wunsch solution (figure 28*b*). It will be noticed that in these and later examples the near bottom current has a positive up-slope component, contrary to observation.

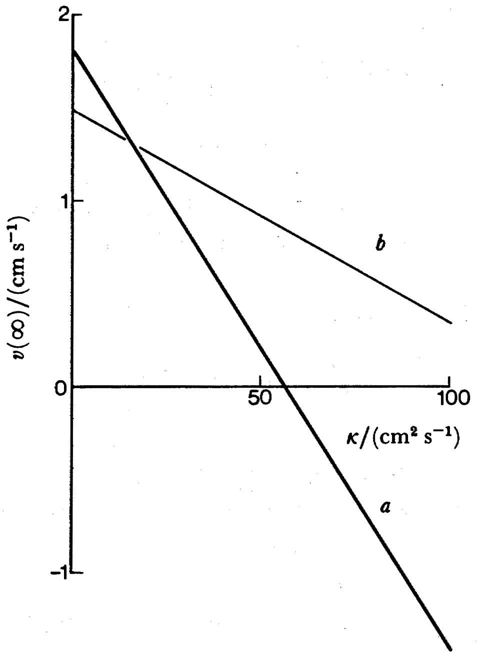

FIGURE 27. Variation of $v(\infty)$ with κ for (*a*) $\alpha = 5°$, $\kappa_1 = 100\ \mathrm{cm^2\ s^{-1}}$, and (*b*) $\alpha = 10°$, $\kappa_1 = 200\ \mathrm{cm^2\ s^{-1}}$, with $h = 50$ m, $N = 10^{-3}\ \mathrm{s^{-1}}$, $f_1 = 10^{-4}\ \mathrm{s^{-1}}$, in the case when the density profile is continuous at $z = h$.

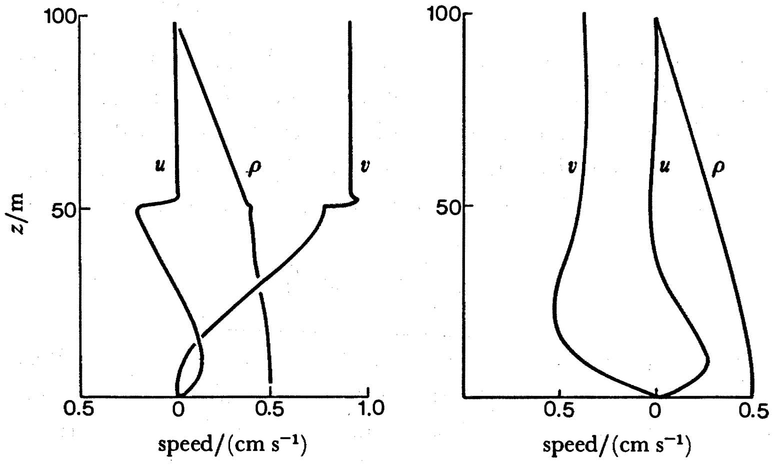

FIGURE 28. Profiles of x-slope and long-slope (u, v) currents and density, ρ, against height, z, for (*a*) $\kappa = 0.5\ \mathrm{cm^2\ s^{-1}}$ and (*b*) $\kappa = 80\ \mathrm{cm^2\ s^{-1}}$, and $\alpha = 5°$, $\kappa_1 = 100\ \mathrm{cm^2\ s^{-1}}$, $h = 50$ m, $N = 10^{-3}\ \mathrm{s^{-1}}$ and $f_1 = 10^{-4}\ \mathrm{s^{-1}}$ in the case when the density profile is continuous at $z = h$.

The values of $v(\infty)$ that give statically stable density profiles with κ specified (here $0.5\ \mathrm{cm^2\ s^{-1}}$) but allowing for discontinuities in ρ (solution class (*b*)), are shown as a function of bottom slope in figure 29. The upper curve corresponds to stable continuous profiles of density, the solutions shown in figure 28, whereas the lower curve have solutions in which density is discontinuous at $z = h$. Some examples are given in figure 30. The density profile in the bottom layer becomes more uniform as the angle decreases, a feature reminiscent of the observations over the slope in comparison with those above an abyssal plain (see §§2.1 and 3.2, and figure 5). At $\alpha = 10°$, an increase in the layer depth, h, raises the band of stable currents, whereas increase in κ lowers the band. At very small angles the band takes solely negative values of $v(\infty)$.

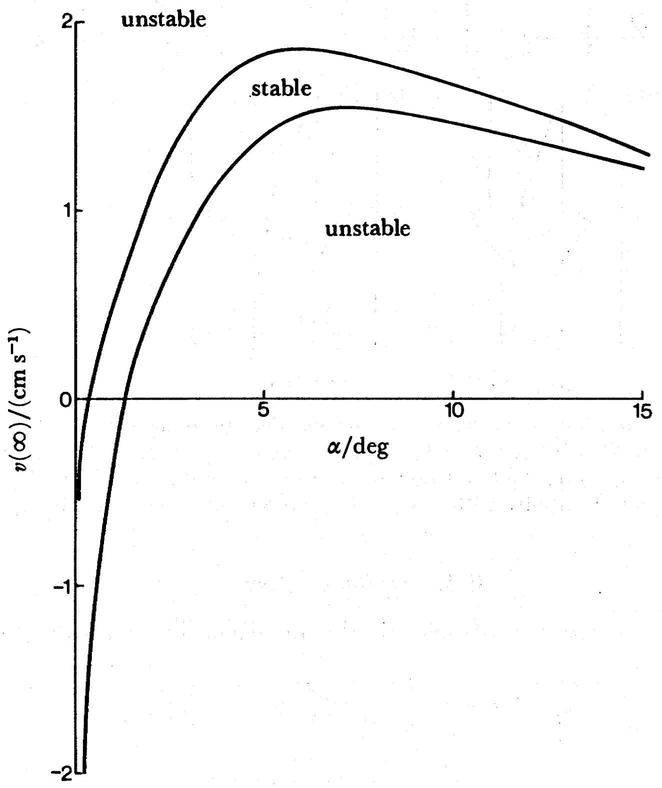

FIGURE 29. The values of $v(\infty)$ for which statically stable solutions exist, as a function of α, for $\kappa_1 = 100\ \mathrm{cm^2\ s^{-1}}$, $\kappa = 0.5\ \mathrm{cm^2\ s^{-1}}$, $h = 50$ m, $N = 10^{-2}\ \mathrm{s^{-1}}$ and $f_1 = 10^{-4}\ \mathrm{s^{-1}}$.

Figure 29 may be regarded as specifying the range of long-slope flows that force a boundary layer response having stable conditions of stratification. It is customary to relate the turbulent diffusivity to the current via the stress on the boundary, but our approach here is to suppose that the turbulence is otherwise produced (say by breaking internal waves) so that the formulation is self consistent. We might conceive that values of $v(\infty)$ outside the stable band will lead to turbulence, enhanced values of diffusivity, and a self-regulating boundary structure. In the model, static instability occurs near $z = h$, the upper edge of the boundary layer (figure 30*d*, *e*) suggesting that values of $v(\infty)$ beyond the stable range would result in entrainment of fluid and a change in the layer thickness. The observed magnitude of the slope current is in order of magnitude agreement with the range for which the model predicts stability.

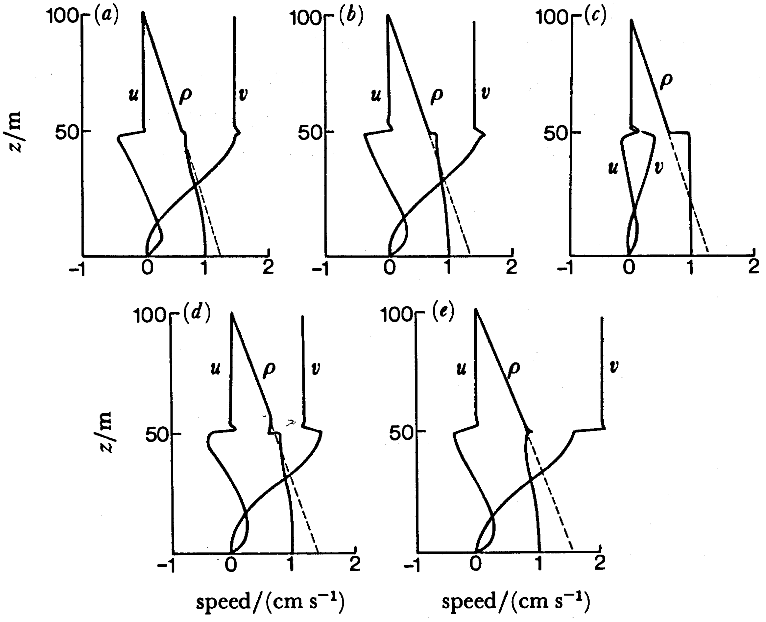

FIGURE 30. Profiles of x-slope and long-slope (u, v) currents and density, ρ, against height, z for $\kappa_1 = 100\ \mathrm{cm^2\,s^{-1}}$, $\kappa = 0.5\ \mathrm{cm^2\,s^{-1}}$, $h = 50$ m, $N = 10^{-3}\ \mathrm{s^{-1}}$, $f_1 = 10^{-4}\ \mathrm{s^{-1}}$, at slope angles, α, of (*a*) 10°, (*b*), (*d*) and (*e*) 5°, and (*c*) 1°. (*a*) (*b*) and (*c*) are for $v(\infty)$ on the lower boundary of the stability curve of figure 29, and (*d*) and (*e*) are below and above the band of stability with $v(\infty) = 1.2$ and $2.0\ \mathrm{cm\,s^{-1}}$ respectively.

6.2. *Oscillatory flows*

We notice that exact periodic solutions are also possible. The equations of motion are

$$\frac{\partial u}{\partial t} - f_1 v = -\frac{1}{\rho_0}\frac{\partial p}{\partial x} - g\frac{\rho}{\rho_0}\sin\alpha + \nu\frac{\partial^2 u}{\partial z^2}, \tag{22}$$

$$\frac{\partial v}{\partial t} + f_1 u = \nu\frac{\partial^2 v}{\partial z^2}, \tag{23}$$

and

$$2\Omega_x v - 2\Omega_y u = -\frac{1}{\rho_0}\frac{\partial p}{\partial z} - \frac{g\rho}{\rho_0}\cos\alpha, \tag{24}$$

where the angular velocity is $(\Omega_x, \Omega_y, \Omega)$, p is the pressure and we have assumed that variables u, v, γ are now functions of z and t only and that there is no y-variation. The advection–diffusion equation for density is

$$\frac{\partial \rho}{\partial t} + u\frac{\partial \rho}{\partial x} = \kappa\rho_0\frac{\partial^2\gamma}{\partial z^2}. \tag{25}$$

Now Phillips's solution (independent of time) is an exact solution that satisfies the above equations. Recalling that $\partial\rho/\partial x = -\beta\rho_0 \sin\alpha$, we see that the equations are linear so that we can add Phillips's solution to a solution of these equations, satisfying the condition $\partial\rho/\partial z = 0$ at $z = 0$. A solution is found by eliminating p and supposing that u, v, γ are proportional to $\exp(-\mathrm{i}\sigma t)$. The boundary conditions are $u = v = \gamma' = 0$ at $z = 0$, and we require a bounded solution at infinity. If we suppose further, for simplicity, that the Prandtl number, ν/κ, is unity, then the solution is of the form

$$u = (B\,\mathrm{e}^{-(1-\mathrm{i}s)b_+z} + D\,\mathrm{e}^{-(1-\mathrm{i})b_-z} + \mathrm{i}C)\,\mathrm{e}^{-\mathrm{i}\sigma t}, \tag{26}$$

$$v = \left(\frac{sBi}{2q^2} f_1\, \mathrm{e}^{-(1-\mathrm{i}s)\,b_+ z} - \frac{Di}{2q^2} f_1\, \mathrm{e}^{-(1-\mathrm{i})\,b_- z} + F\, \mathrm{e}^{-(1-\mathrm{i})\sqrt{(\sigma/2\nu)}z} + \frac{C}{\sigma} f_1\right) \mathrm{e}^{-\mathrm{i}\sigma t}, \tag{27}$$

$$\gamma = \left(\frac{-sBi}{2q^2} \beta \sin\alpha\, \mathrm{e}^{-(1-\mathrm{i}s)\,b_+ z} + \frac{sDi}{2q^2} \beta \sin\alpha\, \mathrm{e}^{-(1-\mathrm{i})\,b_- z} + \frac{f_1 F}{g \sin\alpha}\, \mathrm{e}^{-(1-\mathrm{i})\sqrt{(\sigma/2\nu)}z} - \frac{\beta \sin\alpha}{\sigma} C\right) \mathrm{e}^{-\mathrm{i}\sigma t}, \tag{28}$$

where real parts are to be taken and the set of solutions 12–14 must be added. The complex constants B, D and F can be found in terms of the constant C from the boundary conditions, $s = +1$ or -1 depending on whether σ is greater than or less than critical frequency, $\sigma_c = (f_1^2 + N^2 \sin^2\alpha)^{\frac{1}{2}}$, and $b_\pm = \sqrt{[(\sigma \pm 2q^2)/2\nu]}$, $s = +1$, or $b_\pm = \sqrt{[(2q^2 \mp \sigma)/2\nu]}$, $s = -1$. We have chosen to specify the long-slope oscillatory component, v, at infinity; $v \to V \cos\sigma t$ as $z \to \infty$. The constants specified in terms of V are given in Appendix B.

The solution represents the local response of the boundary layer to forcing by an external wave field. When the amplitude of the motion, determined by V, exceeds a critical value, V_c, the vertical density gradient in the boundary layer becomes positive for some values of z. We

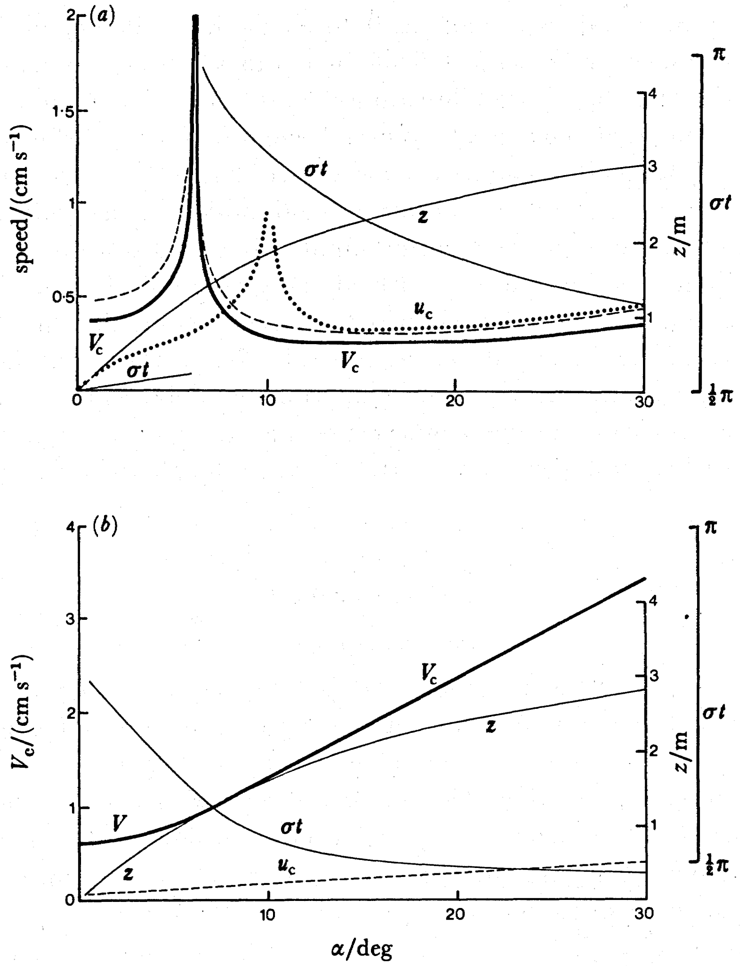

FIGURE 31. The magnitude of the minimum oscillatory velocity V_c (broken line) and U_c far from the slope required to produce conditions of static instability as a function of slope angle for (a) M_2 tidal, (b) 5.45 day period oscillations, with $\kappa = 100$ cm^2 s^{-1}, $N = 10^{-3}$ s^{-1}, $f_1 = 10^{-4}$ s^{-1}. Also shown are the height z and the phase, σt, at which static instability occurs. In (a) the up-slope component required to give static instability when $f_1 = 0$ is shown by a dotted line.

have examined the static stability of the solution due to forcing at semidiurnal and periods of 5.45 days (figure 31). The currents required to initiate conditions of static instability are generally small in comparison with those observed (see figures 10*a* and 20). At M_2 frequencies and for a bottom slope of the experiment, 3–4°, the magnitude of the critical longshore current is about 0.45 cm s^{-1} (the corresponding up-slope current is $U_c \approx \sigma V_c/f$, about 0.55 cm s^{-1}) and the phase is near 90° so that the flow outside the boundary layer is mainly up-slope. This is approximately when mixing is found to occur (see figures 20 and 24) although a more sophisticated model, perhaps along the lines of that described in §6.1 is required before close comparison is justified. For $\sigma > f$, there is a critical slope angle at which σ is equal to the critical frequency and where the solutions are singular and the phase changes abruptly. At M_2, rotation is stabilizing at small slope angles, in that it increases the amplitude of the up-slope flow necessary to produce instability, but it is destabilizing at larger angles ($\alpha > 8.1°$, see figure 31*a*) although only marginally so for slope angles exceeding 15°. It is also marginally destabilizing in the same sense for $1 < \alpha° \leqslant 30$ at periods of 5.45 days.

It seems possible that this boundary layer instability is the source of the layers found by Hart (1971) in laboratory observations of motions induced by an oscillatory inclined plane in a stratified fluid. In making comparison with field observations, however, other effects should be accounted for. Kelvin–Helmholtz instability, an Ekman-layer instability, flow separation over rough topography or internal wave breaking by reflection may set in before static instability occurs in the boundary layer. It should also be recognized that even though conditions of static instability may be achieved, the flow will not develop motions as a result of the release of potential energy until an appropriate Rayleigh number is exceeded at some value of $V > V_c$. Finally we acknowledge that the value of κ selected to display results in figure 31 and taken to be typical of observations may include a contribution from the instability itself. These factors, and the others neglected such as turbulence generated by the shear stress at the boundary and the effect of rough topography, make precise comparison with observations impossible. There is nevertheless some significance in the magnitude of the currents necessary to produce instability, the height at which it appears, and particularly, in the physics of the phenomena.

7. DISCUSSION

7.1. *Mean flows*

Figure 8 appears to provide evidence for a poleward-going mean slope current of limited height that rotates anticlockwise as depth increases towards the bottom. The evidence presented in §3.3 suggests that on average the current is in geostrophic balance.

We must, however, express caution. The eulerian measurements are insufficient to provide inequivocal evidence of the existence of lagrangian flows. Although the M_2 long-slope component is largely barotropic (figure 20), the analysis of the *x*-slope current and temperatures demonstrates that a significant baroclinic component is present near the slope. The slope of the M_2 internal group velocity, β, is (from (2)) about 6.8°, exceeding the local slope, α (see figure 2). Phase propagation appears to be on-slope (figure 18), and the downward phase propagation appears to indicate upward group velocity from a local source (perhaps an interaction between the topography and the barotropic motion (Cox & Sandstrom 1962; Baines 1974; Bell 1975) or because of the local reflection of incident internal waves of M_2

frequency propagating from some remote source. There is theoretical evidence of eulerian-mean x-slope flows in internal gravity waves as they reflect from topography (Wunsch 1971) where no mean lagrangian flows occur. In particular, the up-slope going tidal oscillation would contribute to a mean off-shore eulerian component in the lower part of the water column which, using the equations given by Thorpe (1987; Appendix A) and the estimates of wave amplitude observed in figure 22, would amount to about 0.8 cm s^{-1} at 10 m off the bottom. The waves may also lead to a set-up or set-down of isopycnal surfaces as well as to the apparent up-slope and long-slope buoyancy fluxes referred to in §4.4. It will be necessary to include these effects, as well as those mentioned in §6.1, to provide a complete explanation of the mean motion in the boundary layer.

7.2. *Long-period variability*

The 5–6 day fluctuations advance with the slope to their right, a feature of long wavelength coastally trapped or Kelvin waves. The most perplexing feature of the 5.45 day variation discussed in §4.3 is the off-slope phase shift over a scale less than half the local internal Rossby radius, indicating that phase lines are not at right angles to the slope as in, for example, barotropic Kelvin waves, but are at quite an acute angle with lines of constant phase being roughly north–south. This is reminiscent of the structure of eddies seen in density current flows (see, for example, Stern *et al.* 1982) or in baroclinic instability (Griffiths & Linden 1981). However, the northwesterly phase speed of 13 cm s^{-1} (if correctly estimated; there is some scope for uncertainty in estimating the phase differences by factors in 360°) exceeds the speed of the boundary current and, although suggesting baroclinic motions, appears to exclude baroclinic or other instability phenomena associated with a critical layer in the mean current, and to favour a wave-like motion. A class of coastally trapped or modified Kelvin waves (LeBlond & Mysak 1978; Huthnance 1978) remain a possibility, but these appear generally not to have constant phase lines that lie at angles acute to the slope, and on-slope or off-slope propagation seems more likely. The frequency is lower than the local value of $N \sin \alpha$, that of the Rhines (1970) waves on a slope. A more definitive identification of the motion must await further observations.

7.3. *Short-period variability*

The 'pictures' of the temperature field in the layer near the slope (figures 22 and 23) reveal a variable structure with, at times, frequent and persistent inversions over vertical scales comparable to those measured by CTD (§2.2). These appear to be caused by an instability of the boundary layer that occurs with M_2 tidal period over a scale exceeding that predicted from a formula based on the turbulence produced by shear stress alone (for example, by (1)). The rate of dissipation of turbulence is estimated to exceed the supply from the working of the shear stress on the boundary (§5.5). The nature of the instability, whether from internal wave breaking or some boundary-layer instability, has been discussed at some length (§§5.5 and 6.2) but cannot be unequivocally determined from the present observations. The boundary layer is of a type to which insufficient attention has been given in the past. Longer duration observations with BERTHA (§5.2) closer to the sea bed are planned to identify the source of the inversions. It would also be valuable to use more direct methods to measure the rate of dissipation of turbulent kinetic energy and to compare them with the indirect methods by using CTD observed 'displacements' described here.

Dr C. H. Clayson designed BERTHA and has been responsible for its testing and operation at sea. I am indebted to Dr J. Gould for recovering moorings, Mr I. Waddington for calibration and preparation of instruments, Dr P. Saunders for advice about calibration and analysis and for providing estimates of tidal currents based on Schwiderski's model, and to Mr M. White and Mr P. Haines for assistance in data analysis and for producing figures 2 and 4. Professor M. S. Longuet-Higgins provided the estimate of run length mentioned in §5.3 and verified it experimentally by tossing a coin. I thank the Master and Crew of *RRS Challenger* for their help and cooperation.

Appendix A. The apparent flux of density by wave motions

(*a*) *Barotropic Kelvin waves*

Consider a baroclinic Kelvin wave (LeBlond & Mysak 1978) in a fluid of constant buoyancy frequency, N, that is bonded by a vertical wall at $x = 0$ and between horizontal planes at $z = 0, h$. The Kelvin-wave solution in $x < 0$ with current components (u, v, w) and $w = 0$ at $z = 0, h$, is $u = 0$, $v = v_0\, \mathrm{e}^{kx} \cos mz \sin(ly - \sigma t)$, $w = -(lv_0/m)\, \mathrm{e}^{kx} \sin mz \cos(ly - \sigma t)$ with density $\rho_0[1 - (N^2/g)\, z + \rho]$, where $\rho = (N^2 v_0\, l/g\sigma m)\, \mathrm{e}^{kx} \sin mz \sin(ly - \sigma t)$, v_0 is constant, $m = n\pi/h$, with $n = 1, 2, 3, \ldots$, $k = fl/\sigma$ and $\sigma^2 = N^2 l^2/(m^2 + l^2)$. Although $\overline{w\rho} = 0$ we find $\overline{v\rho} = (v_0^2\, l N^2/4mg\sigma)\, \mathrm{e}^{2kx} \sin 2mz$, so that although the vertical flux of density (or, if $\rho \propto -T$, of temperature) is zero, for sufficiently small, but positive, z there is an apparent (poleward) flux of density (equatorward flux of heat). (The vertically integrated flux is zero.) This apparent flux is not associated with a mean drift. The second-order eulerian current components are

$$(klv_0^2/\sigma(k^2 + l^2))\, [l(\exp(2lx) - \exp(2kx)) \sin 2(ly - \sigma t), (l \exp(2lx) - k \exp(2kx)) \cos 2(ly - \sigma t), 0]$$

and their average is zero. The Stokes drift is also zero, as can be shown by evaluating $\int \boldsymbol{u}\, \mathrm{d}t \cdot \nabla v$ (see Longuet-Higgins 1969), so that the lagrangian drift is zero. The particles have no mean y-motion and so, following the motion of a particle of fluid, and recalling that (consistent with the model) there is no heat conduction or diffusion, there is no real flux of density (or of heat) along the slope. The apparent flux near $z = 0$ is because particles in the wave motion are raised as they move in the positive y-direction, giving a positive fluctuation in ρ, and lowered with a negative ρ fluctuation as they move in the negative y-direction, thus producing a net positive value of $\overline{v\rho}$.

The magnitude of the apparent flux of heat can be estimated. If the density can be written locally as $\rho_0[1 - \alpha_1(zT_{0,z} + T) + \beta(zS_{0,z} + S)]$ where $T_{0,z}$ and $S_{0,z}$ are the vertical mean temperature and salinity gradients, and T and S are the fluctuations in temperature and salinity, and if R_ρ is constant so that $\beta S_{0,z} = R_\rho^{-1} \alpha_1 T_{0,z}$ and $\beta S = R_\rho^{-1} \alpha_1 T$, then $N^2/g = \alpha_1 T_{0,z}(1 - R_\rho^{-1})$, $\rho = -\alpha_1 T(1 - R_\rho^{-1})$ and $|\overline{vT}| = -v_0^2 l T_{0,z}/4m\sigma$. In the observational area, $v_0 \sim 0.06\ \mathrm{m\ s^{-1}}$ and at M_2 frequencies $\sigma = 1.4 \times 10^{-4}\ \mathrm{rad\ s^{-1}}$, and so $|\overline{vT}| = -4 \times 10^{-3}(l/m)$ ($\mathrm{K\ m\ s^{-1}}$). This is comparable with the observed values F_v if $l/m \sim 0.04$, that is if the long-slope wavelength of the baroclinic Kelvin waves is about 25 times greater than the vertical wavelength.

(*b*) *Inertial gravity waves*

For the barotropic Kelvin wave there is no long slope, no up-slope flux and no drift that might carry a heat flux. We now consider the reflection of inertial gravity waves from a uniform slope. The incident wave solution in an infinite fluid is $u = -am \sin\phi$, $v = (fam/\sigma) \cos\phi$,

$w = ak \sin\phi$, $\rho = (N^2ak/g\sigma)\cos\phi$, where $\phi = kx+mz-\sigma t$ and $\sigma^2 = (N^2k^2+f^2m^2)/(k^2+m^2)$. This is an exact solution to the inviscid, non-diffusive, Boussinesq equation with density $\rho_0(1-(N^2/g)\,z+\rho)$, where N is again constant. The wave propagates in the $x = z$ plane, $\overline{u\rho} = \overline{w\rho} = 0$, but $\overline{v\rho} = N^2a^2fkm/2g\sigma^2$, is non-zero. There is no eulerian or lagrangian drift. The linear solution for wave reflection from uniform slope inclined at an angle α and normal to the plane of motion of the incident wave is

$$u = -a(m\sin\phi - m_{\mathrm{r}}\sin\phi_{\mathrm{r}}),$$

$$v = (af/\sigma)\,[(m\cos\alpha+k\sin\alpha)\cos\phi-(m_{\mathrm{r}}\cos\alpha+k\sin\alpha)\cos\phi_{\mathrm{r}}],$$

$$w = ak(\sin\phi-\sin\phi_{\mathrm{r}}),$$

$$\rho = N^2a/g\sigma\,[(k\cos\alpha-m\sin\alpha)\cos\phi-(k\cos\alpha-m_{\mathrm{r}}\sin\alpha)\cos\phi_{\mathrm{r}}],$$

where the x- and z-axes are taken up and normal to the slope, $m_{\mathrm{r}} = m-k\sin 2\beta/(\sin^2\beta-\sin^2\alpha)$ is the z-wavenumber of the reflected wave, $\phi_{\mathrm{r}} = kx+m_{\mathrm{r}}z-\sigma t$ and $\sin\beta = [(\sigma^2-f^2)/(N^2-f^2)]^{\frac{1}{2}}$ (see Thorpe 1987; the y- and z-components of the Stokes drift are zero but, as mentioned in §7.1, the x-component is non-zero). There is an on-slope flux $\rho(u\cos\alpha-w\sin\alpha) = (a^2N^2k\sin 2\beta/2g\sigma\gamma)\sin(kz\sin 2\beta/\gamma)$, where $\gamma = \sin^2\beta-\sin^2\alpha$, which is positive for small z. There is also a long-slope flux $\overline{v\rho} = -a^2k^2N^2f\sin 2\alpha\sin^2 2\beta/(4g\gamma^2\sigma^2)$, which is negative and independent of z. The long-slope eulerian drift is indeterminate at second order (Wunsch 1971).

It may be shown that there is no apparent heat flux for baroclinic Rossby waves between fixed parallel upper and lower boundaries.

APPENDIX B. COEFFICIENTS IN EQUATIONS FOR VELOCITY AND DENSITY FLUCTUATIONS

The coefficients in (26) to (28) are

(*a*) $s = +1$, $\sigma > \sigma_{\mathrm{c}}$;

$$F = Vf_1\left[b_+\left(\frac{\sigma}{f_1}-1\right)-b_-\left(\frac{\sigma}{f_1}+1\right)\right]\Bigg/\left[2q^2\left(b_++b_-+2f_1^2\sqrt{\frac{\sigma}{2\nu}}\Big/N^2\sin^2\alpha\right)\right]$$

$$B = \frac{q^2F}{f_1}+\tfrac{1}{2}V\left(1-\frac{\sigma}{f_1}\right),\quad D = -\frac{1}{2f_1}[2q^2+V_0(\sigma+f_1)],$$

$$C = \frac{V}{f_1}(\sigma^2-4q^4).$$

(*b*) $s = -1$, $\sigma < \sigma_{\mathrm{c}}$;

$$D \equiv D_{\mathrm{r}}+\mathrm{i}D_{\mathrm{i}} = \frac{V}{Q}\left\{\frac{\sigma}{f_1}b_+b_-+\frac{f_1b_+\surd(\sigma/2\nu)}{N^2\sin^2\alpha}(\sigma+2q^2)\right.$$

$$\left.+\mathrm{i}\left[f\sqrt{\left(\frac{\sigma}{2\nu}\right)}(2q^2-\sigma)\left(b_-+\frac{2f^2\surd(\sigma/2\nu)}{N^2\sin^2\alpha}-\frac{\sigma b_+^2}{f_1}\right)\right]\right\},$$

where

$$Q = b_+^2 + \left(b_- + \frac{2f_1^2\sqrt{(\sigma/2\nu)}}{N^2\sin^2\alpha}\right)^2,$$

$$B \equiv B_\mathrm{r} + \mathrm{i}B_\mathrm{i}, \quad \text{where} \quad B_\mathrm{r} = -D_\mathrm{r} \quad \text{and} \quad B_\mathrm{i} = -\frac{\sigma V}{f_1} - D_\mathrm{i},$$

$$F \equiv F_\mathrm{r} + \mathrm{i}F_\mathrm{i} \quad \text{where} \quad F_\mathrm{r} = \frac{f_1}{q^2}D_\mathrm{i} - \left(1 - \frac{\sigma}{2q^2}\right)V, F_\mathrm{i} = -\frac{fD_\mathrm{r}}{q^2}, \quad \text{and} \quad C = -\frac{V(4q^4 - \sigma^2)}{f_1}.$$

REFERENCES

Armi, L. 1978 Some evidence for boundary mixing in the deep ocean. *J geophys. Res.* **83**, 1971–1979.

Armi, L. & D'Asaro, E. 1980 Flow structures in the benthic ocean. *J. geophys. Res.* **85**, 469–484.

Baines, P. G. 1974 The generation of internal tides over steep continental slopes. *Phil. Trans. R. Soc. Lond.* A**227**, 27–58.

Barbee, W. B., Dworski, J. G., Irish, J. D., Larsen, L. H. & Rattray, M. 1975 Measurements of internal waves of tidal frequency near a continental boundary. *J. geophys. Res.* **80**, 1965–1974.

Bell, T. M. 1975 Topographically generated internal waves in the open ocean. *J. geophys. Res.* **80**, 320–327.

Bird, A. A., Weatherly, G. L. & Wimbush, M. 1982 A study of the bottom boundary layer over the eastward scarp of the Bermuda Rise. *J. geophys. Res.* **87** (C10), 7941–7954.

Cairns, J. L. 1967 Asymmetry of internal tidal waves in shallow coastal waters. *J. geophys. Res.* **72**, 3563–3565.

Caldwell, D. R., Brubaker, J. M. & Neal, V. T. 1978 Thermal microstructure on a lake slope. *Limnol. Oceanogr.* **21**, 372–374.

Cox, C. S. & Sandstrom, H. 1962 Coupling of internal and surface waves in water of variable depth. *J. oceanogr. Soc. Japan* **20**, 499–513.

Crawford, W. R. 1986 A comparison of length scales and decay times of turbulence or stably stratified flaws. *J. phys. Oceanogr.* **16**, 1847–1854.

DeWitt, L. N., Levine, M. D., Paulson, C. A. & Bert, W. V. 1986 Semi-diurnal internal tide in JASIN: obcervation and simulations. *J. geophys. Res.* **91**, 2581–2592.

Dickson, R. R., Gould, W. J., Muller, T. J. and Maillard, C. 1985 Estimates of the mean circulation in the deep (< 2000 m) layer of the eastern North Atlantic. *Prog. Oceanogr.* **14**, 103–127.

Dickson, R. R. & McCave, I. N. 1986 Nepheloid layers on the continental slope west of the Porcupine Bank. *Deep-Sea Res.* **33**, 791–818.

Dillon, T. M. 1982 Vertical overturns: a comparison of Thorpe and Ozmidov length scales. *J. geophys. Res.* **87**, 9601–9613.

Eriksen, C. C. 1982 Observations of internal wave reflexion off sloping bottoms. *J. geophys. Res.* **87**, 525–538.

Eriksen, C. C. 1985 Implications of ocean bottom reflexion for internal wave spectra and mixing. *J. phys. Oceanogr.* **15**, 1145–1159.

Gargett, A. E. & Schmidt, R. W. 1982 Observations of salt fingers in the central waters of the eastern North Pacific. *J. geophys. Res.* **87**, 8017–8029.

Garrett, C. & Munk, W. 1972 Space-time scales of internal waves. *Geophys. Fluid Dyn.* **2**, 225–264.

Gregg, M. C. 1975 Microstructure and intrusions in the California Current. *J. phys. Oceanogr.* **5**, 253–278.

Gregg, M. C., D'Asaro, E. A., Shay, T. J. & Larson, N. 1986 Observations of persistent mixing and near-inertial internal waves. *J. phys. Oceanogr.* **16**, 856–885.

Griffiths, R. W. & Linden, P. F. 1981 The stability of buoyancy-driven coastal currents. *Dyn. atmos. Ocean.* **5**, 281–306.

Hart, J. E. 1971 A possible mechanism for boundary layer mixing and layer formation in a stratified fluid. *J. phys. Oceanogr.* **1**, 258–262.

Heathershaw, A. D. 1979 The turbulent structure of the bottom boundary layer in a tidal current. *Geophys. Jl R. astr. Soc.* **58**, 295–430.

Howard, L. N. 1961 Note on a paper by John W. Miles. *J. Fluid Mech.* **10**, 509–512.

Huthnance, J. M. 1978 On coastally trapped waves; analysis and numerical calculation by inverse interaction. *J. phys. Oceanogr.* **8**, 74–92.

Kundu, P. K. 1976 Ekman veering observed near the ocean bottom. *J. phys. Oceanogr.* **6**, 238–242.

Lazier, J. R. N. 1973 Temporal changes in some fresh water temperature structures. *J. phys. Oceanogr.* **3**, 226–229.

LeBlond, P. H. & Mysak, L. A. 1978 *Waves in the ocean* (602 pages). Amsterdam: Elsevier.

Longuet-Higgins, M. S. 1969 On the transport of mass by time-varying ocean currents. *Deep-Sea Res.* **16**, 431–447.

Longuet-Higgins, M. S. 1970 Longshore currents generated by obliquely incident sea waves, 1. *J. geophys. Res.* **75**, 6778–6789.

McDougall, T. J. & Taylor, J. R. 1984 Flux measurements across a finger interface at low values of the stability ratio. *J. mar. Res.* **42**, 1–14.

Marsden, R. F. 1986 The internal tide on the Georges Bank. *J. mar. Res.* **44**, 35–50.

Miles, J. W. 1961 On the stability of heterogeneous shear flows. *J. Fluid Mech.* **10**, 496–508.

Minster, J.-F. 1985 The two-degree discontinuity as explained by boundary mixing. *J. geophys. Res.* **90**, 8953–8960.

Monin, A. S. & Ozmidov, R. V. 1985 *Turbulence in the Ocean* (247 pages). Dordrecht: D. Reidel.

Munk, W. H. 1966 Abyssal recipes. *Deep-Sea Res.* **13**, 707–730.

Oakey, N. S. 1982 Determination of the rate of dissipation of turbulent energy from simultaneous temperature and velocity shear measurements. *J. phys. Oceanogr.* **12**, 256–271.

Oakey, N. S. 1985 Statistics of mixing parameters in the upper ocean during JASIN Phase 2. *J. phys. Oceanogr.* **15**, 1662–1675.

Osborn, T. R. 1980 Estimates of the local rate of vertical diffusion from dissipation measurements. *J. phys. Oceanogr.* **10**, 83–89.

Phillips, O. M. 1970 On flows induced by diffusion in a stably stratified fluid. *Deep-Sea Res.* **17**, 435–443.

Phillips, O. M., Shyu, J.-H. & Salmun, H. 1986 An experiment on boundary mixing: Mean circulation and transport rates. *J. Fluid Mech.* **173**, 473–499.

Rhines, P. 1970 Edge-, bottom- and Rossby waves in a rotating stratified fluid. *Geophys. Fluid Dyn.* **1**, 273–302.

Sarmiento, J. L., Freely, H. W., Moore, W. S., Bainbridge, A. E. & Broecker, W. S. 1976 The relationship between vertical eddy diffusivity and buoyancy gradient in the deep ocean. *Earth planet. Sci. Lett.* **32**, 357–370.

Saunders, P. M. 1983 Benthic observations on the Madeira Abyssal Plain: currents and dispersion. *J. phys. Oceanogr.* **13**, 1416–1429.

Schmidt, R. W. 1979 The growth rate of supercritical salt fingers. *Deep-Sea Res.* A **26**, 23–40.

Schmidt, R. W. & Evans, D. L. 1978 An estimate of the vertical mixing due to salt fingers based on observations in the North Atlantic Central Water. *J. geophys. Res.* **83**, 2913–2929.

Schwiderski, E. W. 1980*a* Ocean tides, part I: global ocean tidal equations. *Mar. Geodesy* **3**, 161–217.

Schwiderski, E. W. 1980*b* Ocean tides, part II: A hydrodynamic interpolation model. *Mar. Geodesy*, **3**, 219–255.

Smeed, D. A. 1986 Eddies in stratified, rotating fluids. Ph.D. dissertation, University of Cambridge.

Stern, M. E. 1960 The 'salt-fountain' and thermohaline convection. *Tellus* **12**, 172–175.

Stern, M. E. 1975 *Ocean circulation physics*. Int. Geophys. Ser. vol. 19. New York: Academic Press.

Stern, M. E., Whitehead, J. A. & Hua, B.-L. 1982 The intrusion of a density current along the coast of a rotating fluid. *J. Fluid Mech.* **123**, 237–265.

Thorpe, S. A. 1973 Experiments on instability and turbulence in a stratified shear flow. *J. Fluid Mech.* **61**, 731–751.

Thorpe, S. A. 1977 Turbulence and mixing in a Scottish Loch. *Phil. Trans. R. Soc. Lond.* A **286**, 125–181.

Thorpe, S. A. 1983 Benthic observations on the Madeira Abyssal Plain: fronts. *J. phys. Oceanogr.* **13**, 1430–1440.

Thorpe, S. A. 1987 On the reflection of a train of finite amplitude internal gravity waves from a uniform slope. *J. Fluid Mech.* **178**, 279–302.

Turner, J. S. 1973 *Buoyancy effects in fluids* (367 pages). Cambridge University Press.

Weatherly, G. L. & Martin, P. J. 1978 On the structure and dynamics of the oceanic bottom boundary layer. *J. phys. Oceanogr.* **8**, 557–570.

Wunsch, C. 1970 On oceanic boundary mixing. *Deep-Sea Res.* **17**, 293–301.

Wunsch, C. 1971 Note on some Reynolds stress effects on internal waves on slopes. *Deep-Sea Res.* **18**, 583–591.

Wunsch, C. 1976 Geographic variability of the internal wave field: a search for sources and sinks. *J. phys. Oceanogr.* **6**, 471–485.

Wunsch, C. & Hendry, R. 1972 Array measurements of the bottom boundary layer and the internal wave field on the continental slope. *Geophys. Fluid Dyn.* **4**, 101–145.